Inertia driven controlled passive actuation with the Dual-Hemi CVT

A.S.T. (Abhishek) Talele

MSc Report

Committee:
Dr.ir. J.F. Broenink
Dr.ir. T.J.A. de Vries
Dr.ir. R.G.K.M. Aarts
Dr. D. Dresscher

December 2016

052RAM2016

Robotics and Mechatronics
EE-Math-CS
University of Twente
P.O. Box 217
7500 AE Enschede
The Netherlands

Summary

The goal of this assignment is to demonstrate an efficient way of actuation i.e inertia driven controlled passive actuation with the Dual-Hemi CVT (DH-CVT). This research was proposed in order to find an alternative way of actuation to the less efficient electrical motors for actuating the RObotic SEnsors (ROSE).

First, the experimental setup is developed for demonstrating the inertia driven controlled passive actuation. The experimental setup was prepared by suitable modeling of a load disc and flywheel using the compatible ideal physical model (IPM) of the DH-CVT. In this work, a servo controller is designed to achieve the servo motion of the inertia driven DH-CVT by controlling the position of the load. Next, the abstraction layer (torque control layer) is developed to provide the desired ratio signal by using the desired actuation torque. Moreover, an already designed ratio controller that provides the controlled variation of the transmission ratio was introduced in the system. The aforementioned three control layers are implemented to simulate the complete DH-CVT system. The simulation results showed that the load can be actuated using the energy stored in the flywheel and hence the inertia driven CPA can be applied in practice. Furthermore, the inertia driven experiment was designed accordingly. Finally, the unexpected results obtained from the demonstration of the inertia driven CPA experiment inferred that it cannot be successfully demonstrated at the current state of research. Further research discovered that hysteresis in the mechanical system of the DH-CVT restricted the system from achieving the desired transmission ratio, vital for the inertia driven CPA experiment. Also, faster drain of the stored energy showed that friction in the DH-CVT system is significantly higher than the initially considered friction. More research is required to obtain the solution prior to the successful demonstration of the inertia driven CPA.

Contents

1 Introduction

1.1 Context

A large part of the Netherlands is below sea level, this includes the densely populated "Randstad" area. This part would flood without the flood defense system. The flood defense system consists of dikes. Dike inspection is necessary to acquire knowledge about the flood defense system. The goal of the RObotic SEnsor (ROSE) project is developing a team of walking robotic sensors that will autonomously acquire data about the composition, consistency and condition of a dike (Dresscher et al., 2015). Walking robots can overcome rough, irregular and muddy surfaces and are preferred. At University of Twente, the work within the Rose project focuses on developing energy efficient walking robots. Current walking robots are energy inefficient and the tasks required by them are difficult to perform having a limited power supply. Because, they lose energy when actively support the mass of the body and accelerating/decelerating during the locomotion of the legs. In order to overcome this issue, an idea of Inertia driven controlled passive actuation could provide a solution. This concept consists of an inertial element to store the required energy and controlled transfer of energy can be achieved with the Dual Hemi Continuous Variable Transmission (DH-CVT) (Dresscher et al., 2015).

The energy storage element considered in this work is a flywheel. Out of many proposed designs, the DH-CVT concept is chosen because of it's ability to allow the ratio range to both positive and negative values, back-drivability and high efficiency of transmission (Dresscher et al., 2016). The innovative DH-CVT mainly consists of two hemispherical friction wheels which transfers the force between them. The transmission ratio of the DH-CVT depends on the contact angle between both hemispheres. This system arrangement is designed to be energy efficient and actuation forces required for changing the transmission ratio are low. Transmission is used to control the energy flow through the system and hence the state of the load. Thus, this concept of the energy storage by an inertial element and transferring it to the load in a controllable way using a DH-CVT is known as Inertia driven controlled passive actuation with the DH-CVT. This could be an alternative way to delivering the actuation power to the load instead of an electrical actuator. Additionally, by using such a construction, the energy that would otherwise be dissipated, can be recovered in the system by recycling the energy in the mechanical domain as represented pictorially in figure 1.1.

Figure 1.1: Inertia Driven CPA with the DH-CVT, Energy flow diagram

1.2 Motivation and Problem statement

Significant energy losses occur during the legged locomotion when using electrical actuators. Because, electrical motors are not efficient at high torque and legs locomotion need high torque for acceleration and deceleration when actively supporting it's mass [(Dresscher et al., 2014)]. Inertia driven CPA aims at reducing the energy loss by storing the required energy in the Inertial element and using it to drive the state of the load. In this approach, flywheel acts as a primary energy source and servo control is applied separately from the energy source. Hence, the most promising idea is to use DH-CVT and flywheel to perform inertia driven experiments. In order to test this hypothesis, a deeper study is required to design, simulate and finally, demonstrate Inertia Driven Controlled Passive actuation with the DH-CVT.

1.3 Approach

The investigation of Inertia driven controlled passive actuation with DH-CVT starts with an analysis and with gained insight of *drive-train mechanism* and *reconfiguration mechanism*. However, this work focuses only on the development of the *drive-train mechanism* and not on the reconfiguration mechanism since, a controller has already been developed for the *reconfiguration mechanism* [refer (Bonilla, 2016)] and will be used in the simulations and experiments. To model the aforementioned system, the Ideal Physical Model(IPM) representation is used. The IPM representation allows the modeling of necessary connections between the electro-mechanical parts in the system and this is straight forward way to simplify the system than other approaches; hence it is preferred. In this project the detailed model of *DH-CVT* representing all inertial and compliant elements in the system will be developed.

In this work, initially, following a use case approach, a certain flywheel inertia and a disc shaped load inertia will be added in the detailed IPM of DH-CVT, then an IPM will be reduced. Reduced IPM provides us the key analysis of the dynamics of the DH-CVT. After that, the qualitative compatibility of the IPM with reality will be verified. Then, an idea of the approximate energy requirement to drive the complete system can be acquired with and without friction in the system and the possible flywheel parameters will be obtained by simulation trails. The suitability of the obtained flywheel parameters will be confirmed after the deeper simulation study done for the inertia driven CPA experiment.

In this part of the simulation, a servo controller will be designed to control the desired actuation torque to achieve the desired load motion separately based on the dynamics of the Inertia driven CPA. Then, the DH-CVT system consisting of both drive-train mechanism and reconfiguration mechanism will be simulated to gain the insight for the desired load motion and energy flow through the system for the chosen flywheel parameters.

Once the suitability of the flywheel design is confirmed in simulations, 3D models of a flywheel and a disc shaped load will be modeled in the `SOLIDWORKS` environment ensuring that desired design specifications are attained. Then, the experimental setup will be prepared by incorporating the manufactured flywheel and load disc in the setup.

Finally, the experiments will be conducted to observe, whether (1) the desired load motion is achieved and (2) detailed analysis will be done.

1.4 Organization of the Thesis

In the chapter 2, the theoretical background introduces and discusses the relevant previous work and the explains the useful concepts used to fulfill the requirements of this project. Next, a comprehensive IPM model is derived, simplified and verified. Moreover, the flywheel modeling is explained in chapter 3. In chapter 4, the simulation results for complete system are analyzed and insight is gained for the design of the experiment. In chapter 5, experiments and results are explained in details. Finally, chapter 6 presents the conclusion and recommendations.

2 Background Information

This chapter provides relevant information obtained from the literature review. First, the Inertia driven CPA concept is briefly explained. Following that, the design and functionality of the Dual Hemi-CVT system is described. Additionally, an already designed ratio controller for the reconfiguration mechanism of the DH-CVT is implemented, providing the actual ratio. Then, information about plant modeling and reduction techniques are provided. Finally, the procedure used for designing the servo controller required to control the position of the load is described.

2.1 Controlled Passive Actuation (CPA)

The modern incarnation of the passive-dynamic approach to locomotion was effectively invented by Tad McGeer. It introduces the concept of the passive dynamic walking. These passive dynamic walkers were able to walk in a stable fashion without the use of any actuators. Nevertheless, they can be combined easily with active energy input to produce efficient and dexterous walking over a broad range of terrain (Mcgreer, 1990).

A device operating passive dynamically can be efficient because it needs no energy for stabilization or control, only power to recover small losses. The most fundamental cause of this energetic loss is impact, primarily between the feet and the ground (Collins et al., 2001). Adding actuation to passive dynamic walkers results in highly efficient robotic walkers. However, adding electrical actuators provides significant energy loss (Dresscher et al., 2014).

The Controlled Passive Actuation (CPA) is a combination of active and passive systems. It is an alternative way to electrical actuation. This integral approach is presented as minimizing the use of electric actuators and enables absorption and re-use of energy involved at impact. By doing so, the number and size of electric actuators is reduced (Dresscher and Stramigioli, 2013). In general, it aims at reducing the energy flow through electric actuators by actuating with a combination of an energy storage element and a Continuously Variable Transmission (CVT) (Dresscher et al., 2015).

2.2 Design and functionality of the Dual Hemi-CVT

The Dual-Hemi CVT is a new traction based CVT concept specifically thought for achieving the controlled energy transfer to develop the Control Passive Actuation (CPA). This continuous variable transmission consists of two hemi-spherical friction wheels.

2.2.1 Overall mechanical design

As mentioned above, the DH-CVT consists of two hemispherical friction wheels which enable the bi-directional power transmission through the system which allows for the variation of the transmission ratio by changing their mutual contact angle. In order to make this alternation possible, the system makes use of two separate frames: one fixed and a second repositionable according to a desired transmission ratio. Each frame holds one of the friction wheels in place. The mechanical design is explained in detail in [Naves (2014)]. The *Drive-train mechanism* takes care of the frame with the fixed wheel, while the adjustable friction wheel frame is taken care by the *reconfiguration mechanism*. Both of the mechanisms are kinematically decoupled from each other, enabling for energy efficient transmission [(Dresscher et al., 2016)]. The design is explained in details in the upcoming subsections. In the following figures, the *drive-train mechanism* and the *reconfiguration mechanism* are depicted.

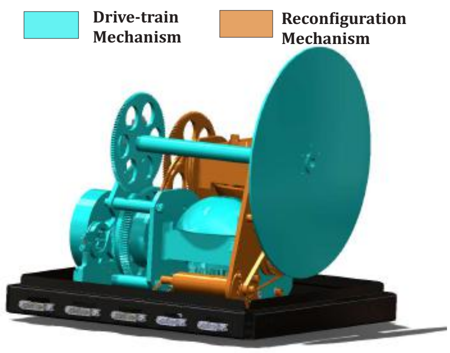

Figure 2.1: DH-CVT mechanical design

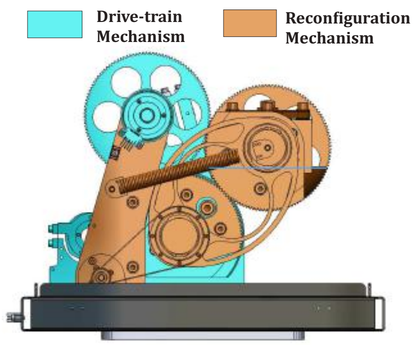

Figure 2.2: Reconfiguration mechanism

2.2.2 Drive-train (Power-train) Mechanism

The drive-train mechanism mainly consists of a planetary gear, a DH-CVT and a mechanical transmissions with fixed ratio. Two safety clutches are mounted on both input and output sides of the mechanism to prevent the overloading of the input and output forces, ultimately preventing overloading of the CVT [(Naves, 2014)]. A load-disc is connected to the output shaft, while a flywheel is connected to the input shaft to store the required energy. The flywheel is shown in Figure 2.1. The other components of the drive-train mechanism are portrayed in Figure 2.3.

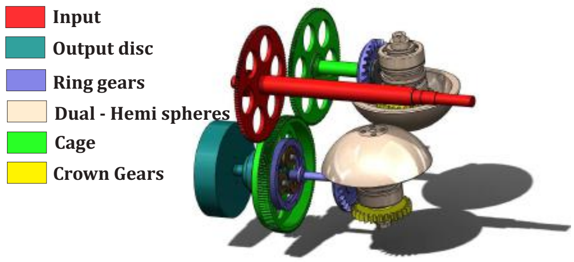

Figure 2.3: Power transmission mechanism of DH-CVT

The Power-split principle is utilized in the system, using a planetary gear to transmit part of the power through the continuous variable transmission, and the rest through a straight mechanical path. It enables efficient bi-directional power transmission throughout the system. The transmission ratio of the power-split CVT (PS-CVT) is directly related to the transmission ratio of the CVT, planetary gearbox and mechanical transmission with fixed ratio [(Dresscher et al., 2016)]. The ring wheel of the planetary gearbox is connected to the fixed friction wheel. Both fixed and mobile friction wheels are connected with the use of ring and crown gears. For the inertia driven system, the sun gear is connected to the output shaft of the mechanism and input is connected to the gear indicated in red color. In contrast with the spring driven system, the input and output connections are of opposite sides [(Bonilla, 2016)].

2.2.3 Reconfiguration mechanism

The reconfiguration mechanism consists of the reconfiguration motor, gravity compensator and mobile frame with friction wheel. The parts of the reconfiguration mechanism are depicted in Figure 2.4.

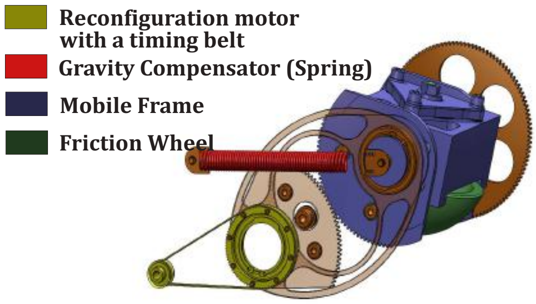

Figure 2.4: Detailed reconfiguration mechanism of the DH-CVT

The reconfiguration motor actuates the reconfiguration mechanism with the help of a timing belt connected to the structure of the mobile frame. The gravity compensator (spring) compensates for the gravitational forces acting on the reconfiguration mechanism and hence reduces the required actuation force of the motor and mobile frame, allowing for the variation in the transmission ratio by rolling the mobile friction wheel over the fixed friction wheel. To guide the frame, and to ensure a proper orientation and alignment, the mobile frame is guided by a rail. Moreover, the design is supported by two flexible arms in order to withstand the contact force between the friction wheels [(Naves, 2014)].

2.2.4 Ratio controller

In the work of [(Bonilla, 2016)], a feed-forward in combination with a feedback ratio controller is designed for controlling the position of the *reconfiguration mechanism*. The reconfiguration mechanism contains non-ideal behaviors, thus a model based control is used so that the controller can modify the model behavior in response to changes in the dynamics of the process. The ratio controller consists of the feed-forward controller which compensates for the residual forces of the gravity compensator and the non-linear friction phenomena. Along with that, a feedback PID controller is designed as a standard rigid mass controller which ensures the robust tracking and disturbance rejection by dealing with the non-idealities of the *reconfiguration mechanism*. The control structure implemented for this ratio controller design can be observed in the following figure:

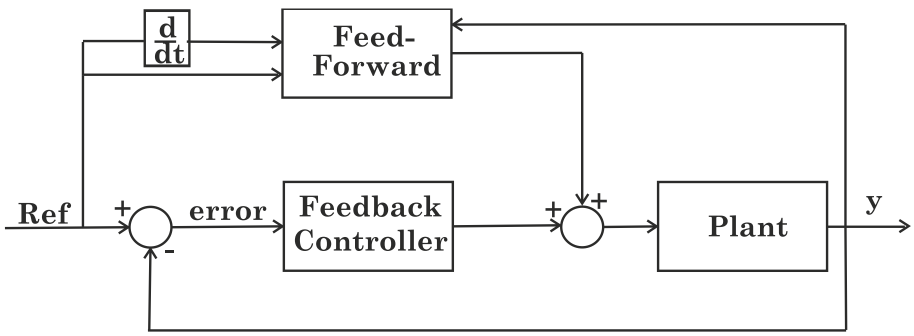

Figure 2.5: Control structure implemented

An improvement of the bandwidth (100 rad/sec) and performance of the ratio controller for the *reconfiguration mechanism* can be observed. It generates the actual ratio for the system and allows the controlled energy transfer through the system, later achieving the desired load motion.

2.3 Plant modeling

Reference: (de Vries, 2014)
Ideal Physical Modeling (IPM) allows detailed physical modeling and provides a quick and insightful way of reduction and simplification procedure. IPM enables the graphical representation of the basic mechanical elements, which resembles their actual physical properties. Nevertheless, this physical modeling helps to understand the dynamics of the system and to analyze the system's behavior. By understanding the dynamics of the system, it also allows us to examine the system with the control theory laws and makes it easier to design a controller.

2.3.1 Model reduction technique

All the elements of the system are taken into account while obtaining the IPM of the system. In order to understand the correct dynamic behavior of the system, it is important to determine the elements providing dominant dynamic behaviors and then reduce the model so that only dominant dynamic behaviors can be analyzed. For the obtained detailed model, the relative importance of model elements cannot be evaluated directly due to the transmissions in the model. Hence, in the IPM, it is desired to perform the model reduction by removing the transmissions from the model, enabling us to identify the effect of each inertial and compliant element in the system by comparing the magnitudes of those elements. This further leads us to discard the less dominant elements from the system by following one of the criteria described below. In our case, 'criterion 1' is used to reduce the plant model.

Criterion 1

• Masses or inertias that are significantly smaller (≈ 0) than the remaining inertias are eliminated.
• Stiffnesses with significantly high values ($\approx \infty$) are considered as rigid connections.

Criterion 2

• Inertias that are infinitely inert ($\approx \infty$) are considered as fixed world.
• Stiffnesses that are very compliant (≈ 0) are considered as not connected.

In this reduction process, it is desired to have a reduced model in terms of the end effector (Load-disc) coordinates. Thus, the transmissions are moved to the input side of the plant (Flywheel) and then eliminated, adjusting their magnitudes according to the transmission ratio.

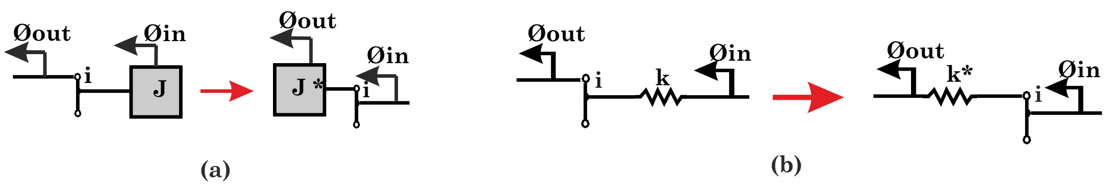

Figure 2.6: Model transformations: (a) Inertia (b) Stiffness

Figure 2.6 describes the model reduction from input to output with the displacement of transmission towards input side. It is possible to observe that J becomes J^*, since its value has been newly calculated according to the transmission ratio. The general relation of the transmission ratio is given as:

$$\boxed{i = \frac{\dot{\phi}_{out}}{\dot{\phi}_{in}}} \tag{2.1}$$

It is mandatory to keep the same energy flow while removing the transmissions in order to avoid the loss of information in the model. This can be explained by means of the kinetic co-energy equations, given as:

$$\boxed{\frac{1}{2}J(\dot{\phi}_{in})^2 = \frac{1}{2}J^*(\dot{\phi}_{out})^2 \longrightarrow J^* = J \times \frac{\dot{\phi}^2_{in}}{\dot{\phi}^2_{out}} \longrightarrow J^* = \frac{J}{i^2}} \tag{2.2}$$

The same energy balance equation applies to the springs as well:

$$\boxed{\frac{1}{2}k(\dot{\phi}_{out})^2 = \frac{1}{2}k^*(\dot{\phi}_{in})^2 \longrightarrow k^* = k \times \frac{\dot{\phi}^2_{out}}{\dot{\phi}^2_{in}} \longrightarrow k^* = \frac{k}{i^2}} \tag{2.3}$$

For the sinks and sources, we only need to adjust the units in terms of the end effector and scale the value. Thus when a transmission is moved to the left side of a source or sink, it is only necessary to divide by the ratio of the transmission.

$$\boxed{F = \frac{\tau}{i} \qquad \text{or} \qquad \tau = \frac{F}{i}} \tag{2.4}$$

2.4 Servo controller design

PD controller structure and algorithm

A PD controller continuously calculates an error value as the difference between a desired set-point and a measured process variable and applies a correction based on proportional and derivative terms. In general, each of these actions has a specific function in motion control: the proportional action provides the desired bandwidth and the derivative action predicts the system's behavior, thus improving settling time and overall stability of the system.

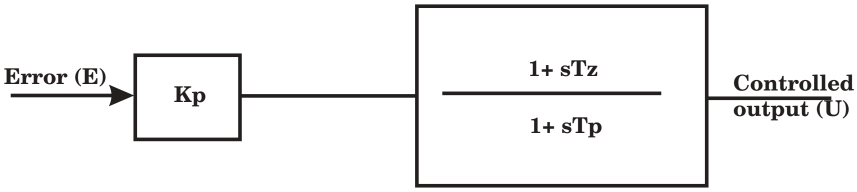

Figure 2.7: PD controller with derivative filter

The transfer function for the PD controller with derivative filter is given as:

$$c(s) = K_p[\frac{1+s\tau_z}{s\tau_p+1}]......(\text{condition}\tau_z > \tau_p) \tag{2.5}$$

In Equation 2.5, τ_z represents the time period $(1/\omega_z)$ at which the damping action begins, τ_p is the time period $(1/\omega_p)$ at which the damping action finishes. Because of the interaction between τ_p and τ_z, rules of thumb have been developed in order to facilitate the tuning of this type of algorithm. These rules help determine the gain K_p, and the values of τ_z and τ_p.

$$K_p = \frac{\omega_c^2 I_{total}}{\sqrt{\beta}} \tag{2.6}$$

$$\tau_z = \sqrt{\beta}\frac{1}{\omega_c} \tag{2.7}$$

$$\tau_p = \frac{1}{\sqrt{\beta}\omega_c} \tag{2.8}$$

A typical value of the derivative gain limitation (β) ranges between 8 to 20.

3 Modeling and design of the experimental setup

In order to understand the dynamic behavior of the DH-CVT, it is desired to develop competent models of the *drive-train mechanism* and the *reconfiguration mechanism* which consists the DH-CVT, as explained in Section [2.2]. In this chapter, a complex and simplified Ideal Physical Modeling procedure is described with the focus on the *drive-train mechanism*, responsible for the power transmission in the system. Additionally, to complete the experimental setup for the inertia driven CPA experiment with the DH-CVT system, the design of the flywheel (input) and a design of a load disc is explained (for details, see Section 2.2.2).

3.1 IPM of the DH-CVT Inertia CPA to load path

This part explains the modeling process of the DH-CVT drive-train mechanism which is responsible for the energy transfer from flywheel (input) to the load (output). The flywheel stores the necessary energy required to drive the load. This IPM model consists of each element of the drive-train mechanism which contributes to the system's performance.

The ideal physical model of the DH-CVT drive-train is representing each element of the drive-train system graphically, where each inertia has a constant value. A connection between any two elements is considered as an infinitely rigid connection, whereas springs (stiffness) are considered as elements without mass. In addition, the transmissions were considered to have 100% efficiency. All element inertias in the system were obtained from the `SOLIDWORKS 3D-CAD` model of the DH-CVT as it was modeled with desired dimensions and suitable material for each element of the mechanism. However, inertia of the new inertial elements, i.e flywheel to be added as an input and load disc as an output, are unknown and necessary to be presumed and added in the graphical model in order to derive the comprehensive IPM of the DH-CVT. Before deriving the IPM model of the DH-CVT system, it is better to understand the overview of the mechanical connections of DH-CVT experimental setup.

3.1.1 Schematic overview of the Inertia driven CPA experimental setup

The schematic overview of the DH-CVT setup is shown in figure 3.1. The IPM derived in the section 3.1.4 is based on the basic mechanical connections of the inertia driven DH-CVT system illustrated in the schematic diagram.

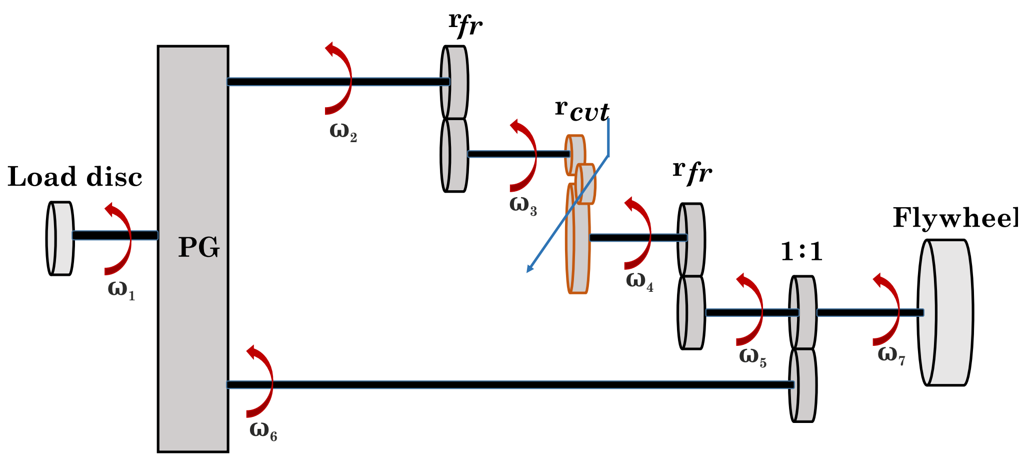

Figure 3.1: Schematic overview of the DH-CVT drive-train

The experimental setup is typically built with a regular continuously variable transmission (CVT), a planetary gear system with differential properties (PG), an input inertial element (flywheel), an output (load disc) and optionally a mechanical transmission with a fixed ratio (FR). Initially, the suitable load inertia and flywheel inertia are assumed intuitively for the modeling purpose.

3.1.2 Initial assumptions

As explained in the final part of Section 3.1, it is essential to add the flywheel inertia and load disc inertia along with the rest of the basic elements of the system, enabling the derivation of the detailed graphical model. The disc shaped flywheel is selected for the DH-CVT experimental setup, since the disc shaped flywheels are suitable for smaller sized machines and easier to manufacture.

Initially, the flywheel's inertia and velocity parameters are hypothetically assumed to store an high amount of energy in the flywheel to drive the system. This is due to the fact that the energy required to drive the system was unknown and presumed to be very high intuitively. Thus, the flywheel's parameters such as a significant value of its inertia 0.25 $Kg.m^2/rad$ and high angular velocity of about 6000 RPM are chosen. High value of the angular velocity provides high amounts of energy content in the flywheel since its kinetic energy is directly proportional to the square of its angular velocity. The energy stored in the flywheel is as follow,

$$E_f = \frac{1}{2} I_f \omega_f^2 = \frac{1}{2} 0.25 \times (6000 \times \frac{\pi}{30})^2 = 49348J \tag{3.1}$$

The energy content computed in Equation 4.16 is very high. In this scenario, It seems unrealistic to speed up the flywheel to 6000 RPM for the existing DH-CVT system. The selected flywheel parameters are used only for modeling purposes at the initial stage. After the model reduction, the reliable parameters are better identified in the upcoming sections by simulation trials of the reduced model. Desired load motion and energy flow results are obtained from the simulation, which gave the insight for selecting the final flywheel parameters in the later part. In short, the choice of feasible flywheel parameters were estimated based on the evaluation of total energy required by the DH-CVT system to provide the desired load behavior.

Similarly, the suitable load mass was considered intuitively as 0.5 Kg. The disc shape of the load was preferred as it is simple to model and easier to manufacture. The corresponding load disc inertia was added into the graphical model. The next subsection 3.1.3 describes the mechanical 3D design of the load disc.

3.1.3 Design considerations for the load disc

In order to get better insight for the load motion and energy flow in the system, it is required to calculate the inertia of the load disc and include it in the detailed IPM derivation of the DH-CVT. Thus, the following design parameters were considered such that the 3D load disc model maintains the mass of $\approx 0.5\ Kg$. The material chosen was aluminum, because it is a light weight and attractive material which has high rate of heat dissipation property. Following Figure 3.11, the 3D load disc modeled in `SOLIDWORKS` environment and the bullet points indicates its specifications.

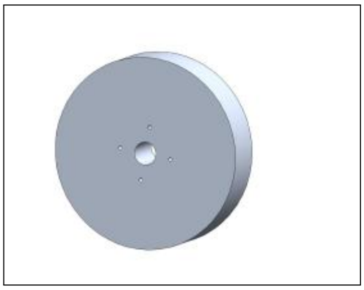

- Material : Aluminium
- density : 2700 Kg/m^3
- Outer radius : 50 mm
- Inner radius : 6 mm
- Thickness : 24 mm
- mass : 0.5 Kg
- Inertia : 6.3×10^{-4} $Kg.m^2/rad$

Figure 3.2: Load Disc

Inertia of the disc shaped load is calculated as:

$$I_l = \frac{1}{2}\pi\rho h(r_o^4 - r_i^4) = 6.3 \times 10^{-4} Kg.m^2/rad. \tag{3.2}$$

Now that we have both the assumed flywheel and a suitable load disc inertia, those were added to the detailed IPM of the DH-CVT shown in Section 3.1.4.

3.1.4 Detailed derivation of IPM of the DH-CVT drive-train

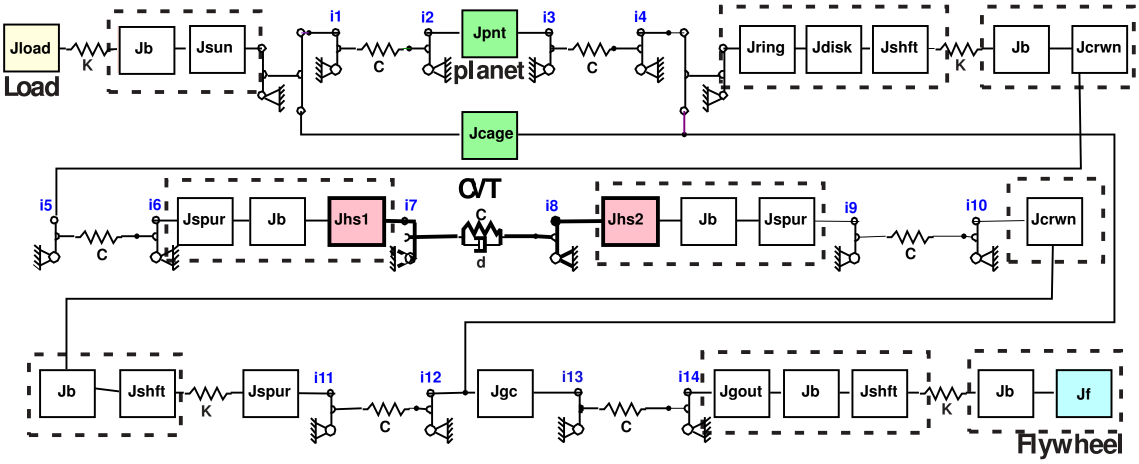

Figure 3.3: DH-CVT with inertia CPA drive-train IPM model

Figure 3.3 depicts the picture of the PS-CVT drive-train ideal IPM including all the inertial and compliant elements in the system. The input of the model is a flywheel inertia and the output a load inertia. The shaft connecting the inertial elements are represented as the rotational stiffnesses. Stiffnesses between the teeth of the gears are linear stiffnesses. As these stiffnesses have very high values, they are considered as rigid connections. The inertias which are directly connected to each other as indicated in the dotted box are summed up together and represented as a single possible dominant inertia.

The inertias and shaft stiffnesses are calculated by referring the DH-CVT's SOLIDWORKS 3D-CAD model mass properties. It provides the used material and dimensions information of each element, making it possible to get all inertias and shear modulus of the material required for stiffness calculation. The stiffness of the shaft is calculated by using the following formula (mitcalc, 2016),

$$K_{shaft} = \frac{\pi * G * D_{shaft}^4}{32 * L_{shaft}} \tag{3.3}$$

Where, K_{shaft} is the rotational stiffness of the shaft, D_{shaft} the diameter of the shaft, L_{shaft} the length of the shaft and G the shear modulus of the material used for the shaft. The inertias and stiffnesses of the IPM are mentioned in Appendix A.

The teeth between the primary and secondary gear connection of each gear are considered to be infinitely stiff as they are made of very stiff materials, and are not subjected to very high loads and input forces. In the next subsection, the detailed model shown in Figure 3.3 is reduced and simplified.

3.1.5 Model reduction and simplification of the DH-CVT drive-train IPM

Model reduction and simplification procedures are explained in Section 2.3. To evaluate the significance of each element in the system, it is important to remove the transmissions from the system keeping the same energy flow. The next step is to get rid of the elements referring to Criterion 1, as described in (2.3.1), because rotational stiffnesses of the shaft and stiffnesses between the teeth of the gears are very high. These stiffnesses can be considered as infinite and hence act as rigid connections between inertias. Thus, it is possible to combine the inertias indicated in the dotted colored boxes, from Figure 3.4, as a single dominant inertia.

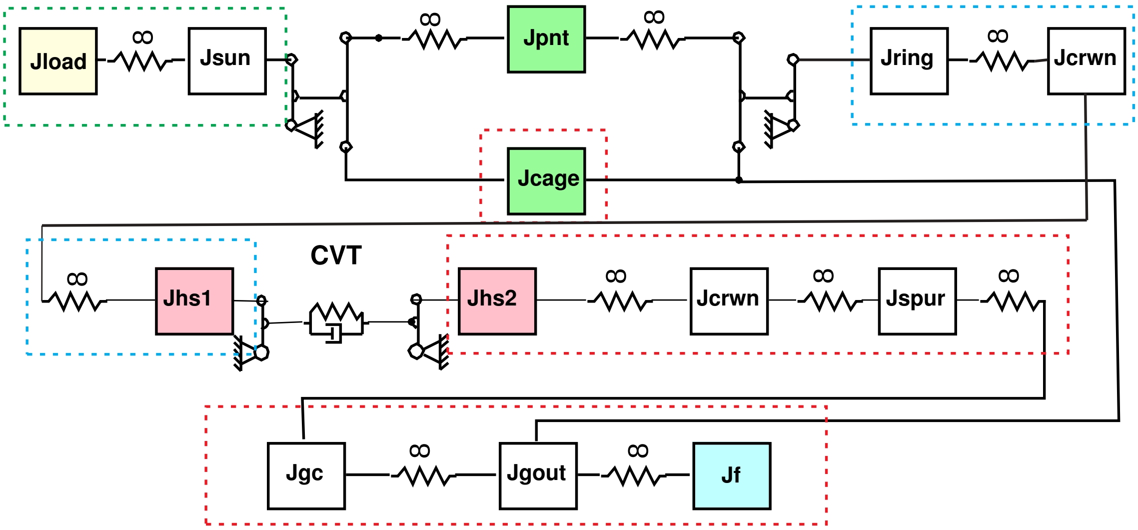

Figure 3.4: DH-CVT drive-train IPM model reduction and simplification

After simplification and reduction of the model in Figure 3.4, the final reduced and simplified system is developed as shown in Figure 3.5. It consists of a flywheel inertia (*Jf*), mobile sphere inertia (*Jhs2*), fixed sphere inertia (*Jhs1*), planetary gear inertia (*Jplnt*), and cage inertia (Jcage) that holds the planet gears and load inertia (*Jload*).

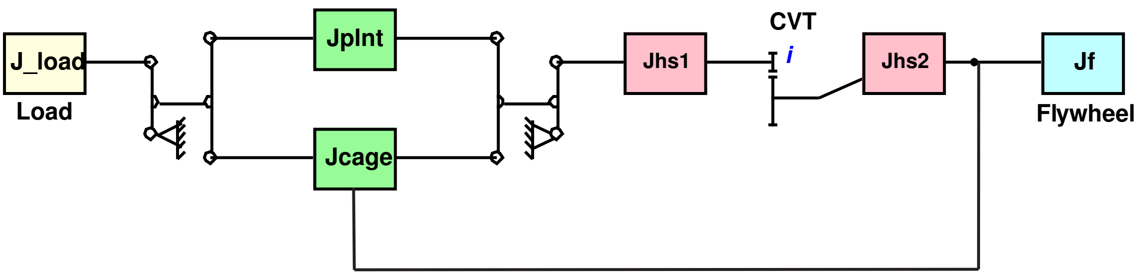

Figure 3.5: Reduced IPM of DH-CVT drive-train Mechanism

The angular velocities of the flywheel (*Jf*), mobile hemi-sphere inertia (*Jhs2*) and cage inertia (*Jcage*) are dependent, as they are rigidly connected to each other. It is further possible to simplify the system in Figure 3.5, by incorporating the summed inertia of the cage inertia (*Jcage*), mobile hemi-sphere inertia (*Jhs2*) and flywheel inertia (*Jf*) into one single dominant inertia. It is addressed as the total flywheel inertia and taken into consideration for further investigation (see Figure 3.6).

Despite the simplification done as above, the connection between the cage inertia (*Jcage*) and flywheel inertia (*Jcage*) sets a complicated loop to solve for the `20-sim` simulator. Additionally, the states of the load inertia, planetary gear inertia and fixed hemi-sphere inertia (*Jhs1*) are dependent on each other, making the system complex as it introduces the discontinuity and difficulties for the simulator to find the solution. Hence, a further computationally optimized model is needed and is obtained by decoupling the states of the load inertia, planetary gear inertia and fixed hemi-sphere inertia with the placement of two spring -damper elements between them. Moreover, the desired causality is also achieved by connecting a third spring -damper element to the CVT transmission. If weak spring dampers are used, a certain amount of (unwanted) displacement would be possible. Hence, low stiffness spring results in larger oscillations in the system and poorer damper characteristics. Thus, to reduce the effect of the spring elements on the system's performance, springs with high stiffness are added. Dampers damp out the oscillations in the system caused by the compliance of the springs. Dampers in mechanical systems provide safety and comfort against dynamical and impact forces. [(Ragavan, 2012)].

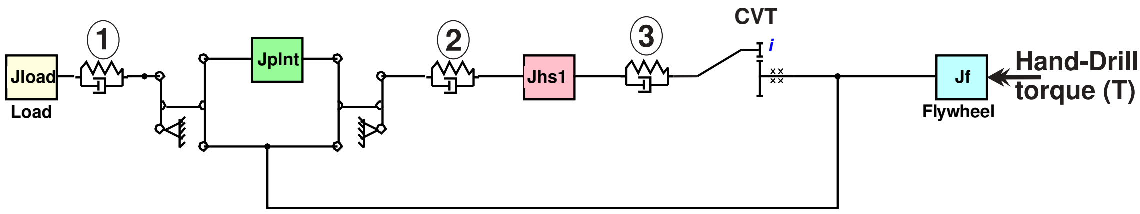

Figure 3.6: Simplified and modified IPM of DH-CVT drive-train Mechanism

Figure 3.6 illustrates the functionality of the DH-CVT. In the current system, the flywheel (*Jf*) is connected to the input shaft which is rotated by the input torque (*T*), given by the hand-drill to store the required amount of energy, to obtain the desired system motion. The stored energy is then transferred to the load through the CVT (*Jhs1*) and the planetary gear (*Jplnt*).

3.1.6 Significance of inertia of planet gear ($Jplnt$) and fixed hemi-sphere ($Jhs1$) :

As explained in Section 2.3, it is necessary to remove the transmission from the system to evaluate the importance of each of its elements. However, fixed transmissions can be removed from the system but not the variable transmission (CVT) because of the continuous change in ratio affects the system's performance. Continuous variation in ratio leads to continuous change in the energy in any inertia in that particular system. Thus, to gain insight about the significance of the planet inertia $Jplnt$ and fixed hemi-sphere inertia ($Jhs1$), the energy required for the load, planet and sphere are compared. Since we know that the load inertia is obviously significant, the energy comparison should give the required insight about the significance of planet and sphere inertias (see fig. 3.7

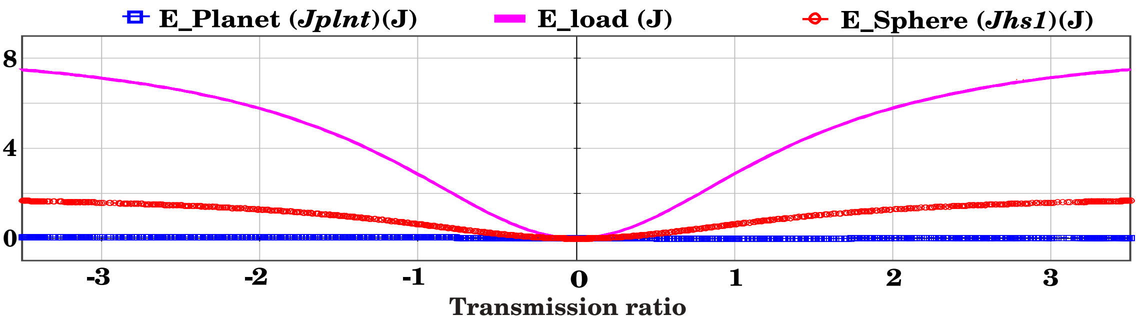

Figure 3.7: Significance of the planet and the fixed hemi-sphere inertia

Figure 3.7 indicates the variation in the energy of both planet inertia ($Jplnt$) and fixed hemi-sphere inertia ($Jhs1$) with respect to the variable transmission ratio. It is clearly observed from Figure 3.7 that the fixed hemi-sphere ($Jhs1$) required 30 % of the energy compared to the energy required for the load. While the planet inertia required almost negligible amount of energy to move over the ratio range of -3.5 to 3.5, it can be inferred that its value in the system is of minimal significance and can then be discarded during the assessment of the total energy required by the DH-CVT system to be in motion. However, it is expected that it should store an infinitesimal amount of energy, as is directly coupled to the input shaft and expected to rotate along with the high speed flywheel. It can be observed from the simulation results mentioned in Section 4.7 of Chapter 4.

3.2 Model verification of the DH-CVT drive-train IPM

After obtaining the reduced IPM of the DH-CVT drive-train, a simulation experiment is conducted to see if the model is performing as desired or not. Simulation is carried introducing the initial flywheel parameters, mentioned in Section 3.1.2 and by considering the efficiency of transmission ratio gearbox as 100%. Variation in the transmission ratio is responsible for the controlled energy transmission in the system and consequently, the change in load position. Thus, the following criteria was expected to be satisfied by the model.

Criteria:

1. Variation in transmission ratio in positive and negative directions should accelerate and decelerate the load.

2. Load should accelerate during positive ratio change and decelerate during negative ratio change.

3. Load should be stand-still i.e load velocity should be zero when the transmission ratio is zero.

4. Energy should be exchanged between flywheel and load in order to achieve the load motion when the transmission ratio is non zero.

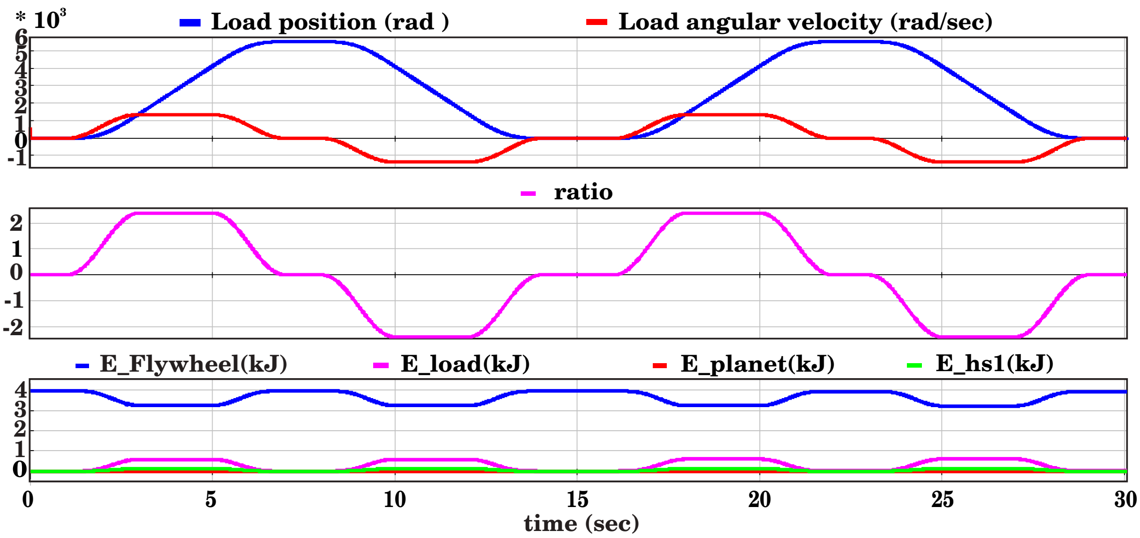

Figure 3.8: DH-CVT Drive-train model verification

Figure 3.8 demonstrates the simulation results obtained for the drive-train model verification. The transmission ratio is modified with the trapezoidal position signal. It is observed that the positive ratio change accelerates the load and negative ratio change decelerates it. This satisfies the first two criteria. Then, it is clearly indicated that load is stationary i.e load velocity is zero when the transmission ratio is zero, which satisfies the third criterion. Next, the energy flow is observed such that the energy stored in the flywheel is transferred to the load in order to accelerate or decelerate the load. Not to mention, the flywheel energy is constantly used by the load when the load is moving at a constant velocity. This satisfies the fourth criterion.

By observing the expected behavior, it is inferred that the reduced simulation model shown in Figure 3.6 correctly represents the key behavior of the physical system. Hence, this simulation model is used for further investigation to derive the reliable flywheel parameters by repeated simulations.

3.3 Design considerations for the flywheel

3.3.1 Approximate flywheel inertia and flywheel velocity parameter computation

As previously mentioned in Section 3.1.2, initially, the flywheel parameters are chosen with inertia corresponding to $0.25 Kg.m^2/rad$ and angular velocity of $6000rpm$ to provide $49348J$ of energy, which are of unrealistic values for the existing DH-CVT system. The rough but reliable flywheel inertia and velocity parameters that provide sufficient amount of energy to observe the expected load behavior are obtained. Several simulation trails of IPM, Figure 3.6, are done to reach a reliable flywheel parameter selection. The flywheel inertia and angular velocity are varied by inspecting the required amount energy for sufficient motion of the system, flywheel energy content and mechanical feasibility of the flywheel with the DH-CVT setup. To check the feasibility of the mechanical design of the required flywheel, the mechanical design parameters are also calculated simultaneously in Section 3.3.2 for respective flywheel inertia and velocity.

After, observing the simulated results for several different combinations of flywheel rotational velocities and inertias, the reliable and supposedly desired flywheel parameters are chosen as *flywheel velocity* $= 350rpm$ and *inertia* $= 0.0155 Kg \cdot m^2/rad$. The energy stored in the flywheel is,

$$E_f = \frac{1}{2} I_f \omega_f^2 \quad = \quad \frac{1}{2} \times 0.0155 \times (350 \times \frac{\pi}{30})^2 \\ = \quad 10.42\text{J} \tag{3.4}$$

Figure 3.10 depicts the energy flow analysis for the final simulation performed in order to select realistic flywheel parameters.

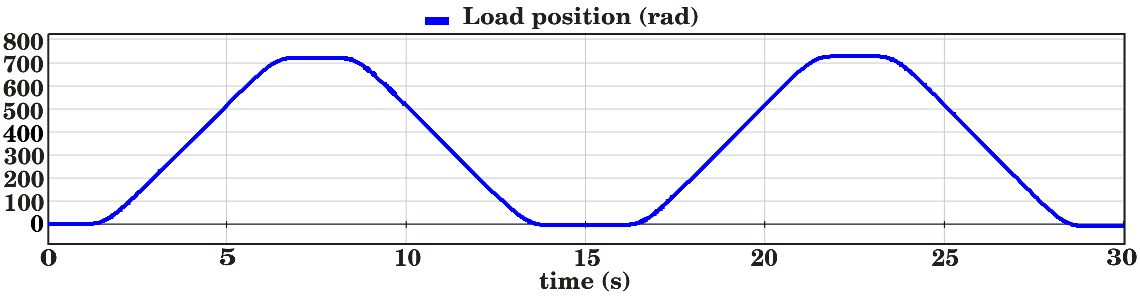

Figure 3.9: Load behavior of the system

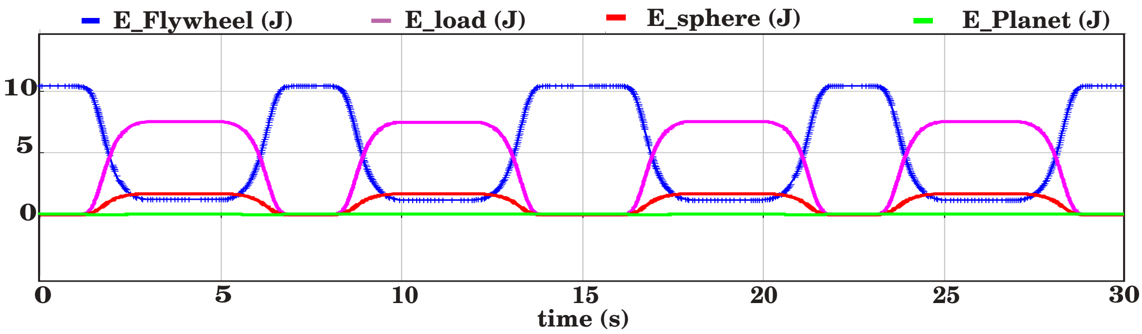

Figure 3.10: Energy flow for the friction-less system

From the above energy response obtained for the loss-less system, it is obvious to observe that the system follows the continuous motion and the consumed energy is restored back to the flywheel when the load in not in motion. The total required amount of energy is calculated by summing up the energy exchange in the load inertia, planet inertia and CVT hemi-sphere inertia while the system is in motion. From the simulated energy flow response in Figure 3.10, the total amount of energy in Equation 3.5 exchanged in the system is compared against the energy supplied by the flywheel. From Figure 3.10, it was possible to know the maximum energy required by individual load, planet and fixed hemi-sphere inertia during the acceleration and deceleration of the load. Next, the approximate energy consumption is calculated for one motion cycle consisting of acceleration and deceleration of the load.

$$\text{Total energy required by the system} = E_{Load} + E_{planet} + E_{sphere} \\ = 7.52 + 0.01 + 1.68 = 9.21\text{J} \tag{3.5}$$

Energy calculated in Equation 3.5 indicates that the energy exchange required for the moving system is approximately $9.21J$ out of the provided flywheel energy ($10.42J$). It gave the appropriate idea that selected flywheel design fulfills the energy requirement such that the system shows the desired motion. The calculated energy provides load angular position of approximately 700 rad, implying that the acceleration of the system is very high as shown in Figure 3.9. The current energy exchange, ($9.21J$), is required because of high angular acceleration for the load. The energy transmission requirement changes based on the acceleration of the load. The load position for the loss-less system is 700 rad, which is a considerably high position that could be observed from the actual experiment. Similarly, the same model, but while considering the friction in the system, provides a considerably high load position as well of 300 rad.

However, the above simulated response is not the desired (controlled) load behavior. Hence, this simulation only provides rough estimates for the flywheel inertia and velocity. Moreover, the observed high load position allows us to presume that the current flywheel model should provide the desired load motion for sufficient amount of time with the controlled energy transmission. Hence, the roughly estimated flywheel model is retested and finalized by observing the desired load motion and controlled energy transmission with the complete DH-CVT simulation model in Chapter 4.

3.3.2 Mechanical design of the flywheel

The mechanical design specifications were calculated simultaneously to the flywheel inertia and velocity parameter estimation with the simulations mentioned in the previous section, Section 3.3.1. Hence, a feasible flywheel mass value was also picked by repeated mechanical design calculations i.e if the flywheel mass is not within the feasible range then the flywheel inertia and velocity that was considered in the previous simulations had to change intuitively to store sufficient amount of energy in the flywheel.

Safety anticipation: After repeated simulation attempts, the flywheel velocity and flywheel inertia are deliberately chosen as low (suitable) to ensure only sufficient amount of energy content in the flywheel and to avoid unnecessary high energy content, important for the setup's safety. The most probable potential failure modes for the flywheel are brittle fracture and ductile rupture. They mostly occur for high speed flywheels (Jack A Collins, 2010). Not to mention, existing DH-CVT have vague input velocity limit depending on the other parts of the system that should not be exceeded. Additionally, the axial load carrying capacity of the input shaft of the DH-CVT setup was also unclear. Hence, the possibility that the excessive flywheel mass may introduce the high bending stress over the power transmission shaft (input shaft) is considered. Before writing the final design specifications, it is important to analyze that the selected flywheel inertia exhibits virtually low mass for the existing DH-CVT setup, to avoid its wear and tear.

Consequently, further steps were taken in this work to model the 3-D flywheel in the `SOLIDWORKS` environment such that a feasible flywheel mass is achieved for that particular inertia.

In our case, the solid disc shaped flywheel is mounted on the input safety clutch with the help of screws. Since the safety clutch is connected to the input shaft and the flywheel is rotating with the shaft but not over the shaft, there is no need of designing the bearings for the flywheel.

To start with the design, it was known that the radius of the safety clutch over which the flywheel is to be mounted is $17mm$ and hence the inner radius of the flywheel should be $r_i = 17mm$ plus tolerance. It was also known that the energy content that the flywheel should store is $E_f = 10.42J$. Following, mechanical design equations (Kamf, 2012) are used to calculate the required geometrical design specifications for the flywheel

$$\begin{aligned} &\text{The inertia of the flywheel} = \frac{1}{2}\pi\rho h(r_o^4 - r_i^4) \rightarrow h = \frac{2I_f}{\pi\rho(r_o^4 - r_i^4)} \\ &\text{Mass of the flywheel} = \rho\pi h(r_o^2 - r_i^2) \\ &\text{Flywheel energy} = \frac{1}{2}I_f\omega_f^2 \end{aligned} \tag{3.6}$$

Where, ρ = density of the material
r_o = outer flywheel radius
h = thickness of the flywheel

Essentially, suitable material is chosen such that material density (ρ) is known, later integrated in the calculation. For practical reasons, the material chosen is BRASS. Brass parts are easy to machine. Moreover, parts made from brass can leverage better balance than other materials, corrosion resistance or attractive appearance as in many decorative parts. Brass parts often get by without a surface finish, saving on cost and delivery time. In addition to that, brass flywheel are less noisier and vibration affected, which helps to balance the flywheel and clutch assembly - making it well suited for the purpose of the experiments. The density of brass is $8500 Kg/m^3$.

The thickness (h) and outer flywheel radius (r_o) are modified by acquiring the desired flywheel inertia $I_f = 0.0155 Kg \cdot m^2/rad$. At the same time, feasible mass of the flywheel is also attained. Obtained realistic mechanical design specifications are mentioned below.

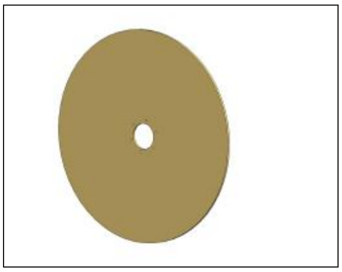

Figure 3.11: 3D Flywheel

- Material : `Brass`
- Material density (ρ) : `8500` Kg/m^3
- Thickness (h) :`3` mm
- Outer flywheel radius (r_o) : `14` cm
- Inner flywheel radius (r_i) : `17` mm
- Mass of flywheel (M_f) : `1.55` Kg
- Inertia of Flywheel (I_f) : `0.0155` $Kg \cdot m^2/rad$
- Flywheel velocity (ω_f) : `350` rpm
- Flywheel Energy (E_f): `10.42` J

Though a practically achievable flywheel is designed by acceptable trade offs between all the flywheel geometrical design variables, it is yet to be identified that the designed flywheel sufficiently provides the energy to the system in order to accomplish the desired load motion. If the complete DH-CVT system illustrates the expected simulation results, it would mean that the flywheel design is sufficient and ready to manufacture. For that reason, extensive simulations are conducted in the next chapter.

3.3.3 Friction model:

It is expected that the DH-CVT with several transmissions in the system shows non-linear friction behavior. In high-performance motion systems, friction can severely deteriorate performance and can introduce negative side effects such as tracking errors, large settling times or limit cycles.

Friction modeling is not part of this assignment, since the static and Coulomb friction model were already modeled for the existing DH-CVT in ((Desscher et al., 2016)). Static and Coulomb friction are modeled for the DH-CVT drive-train considering the non-linear friction phenomena occurring at the planetary gear, ring-crown gears and CVT transmission. From (Desscher et al., 2016), the non-linear behavior is identified at the input of the inertia driven DH-CVT setup. This friction model is introduced in the DH-CVT drive-train IPM as it is expected to give better insight for the real non linear friction phenomena of the system. This friction model gives insight for possible energy losses in the system and helps to determine the required fly-wheel parameters by calculating the required amount of energy in the system.

Referring to the friction model parameters that are identified in ((Dresscher et al., 2016)), the friction model is developed and added in the IPM of the drive-train mechanism. The actual friction model behavior is depicted in Figure 3.12.

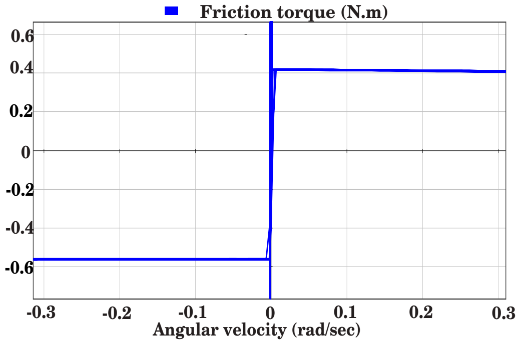

Figure 3.12: Actual friction behavior

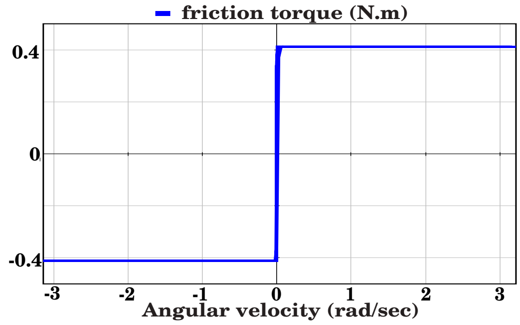

Figure 3.13: Ideal friction behavior

During the simulation, it is noticed that actual friction model introduces a lot of time switches in the system, making it hard to simulate due to its complexity. Therefore, despite the fact that an actual friction model is developed in the ((Dresscher et al., 2016)), illustrating the non-linear behavior in the DH-CVT drive-train, an ideal friction model is used for obtaining the simulation results in Section 4.7 in Chapter 4. Figure 3.13 indicates the ideal friction model behavior. It seems that the actual frictional torque and the ideal frictional torque are of approximately same magnitude, so that the non-linear system behavior can be estimated to analyze the energy loss due to friction. However, it is possible that there might be additional friction acting upon the system since this corresponds to a highly non linear model. Hence, it is important to closely observe the friction phenomena during the experiment.

The simulated and experimental friction phenomena are analyzed and their respective effects are predicted in the next chapters.

3.4 IPM of the reconfiguration mechanism

In this work, it is necessary to understand the dynamics of the reconfiguration mechanism along with the drive-train mechanism, thus an IPM for the reconfiguration mechanism is developed. It is previously described in Section 2.2.3 that the reconfiguration mechanism consists of a reconfiguration actuation motor as input, gearbox for motor, belt-drive transmission gear, lever, gravity compensator and a mobile hemi-sphere mass (load mass) as output. A gravity compensator is added to compensate for the gravitational forces acting on the reconfiguration mechanism. The `SOLIDWORKS 3D-CAD` model for the reconfiguration mechanism is shown in Figure 2.4:

3.4.1 Detailed IPM of the reconfiguration mechanism

Again, the required constant values of inertias are obtained from the mass properties of the `SOLIDWORKS 3D-CAD` model for the DH-CVT. IPM reduction and simplification of reconfiguration systems is also done using the same approach as DH-CVT drive-train model reduction, see Section 3.1.

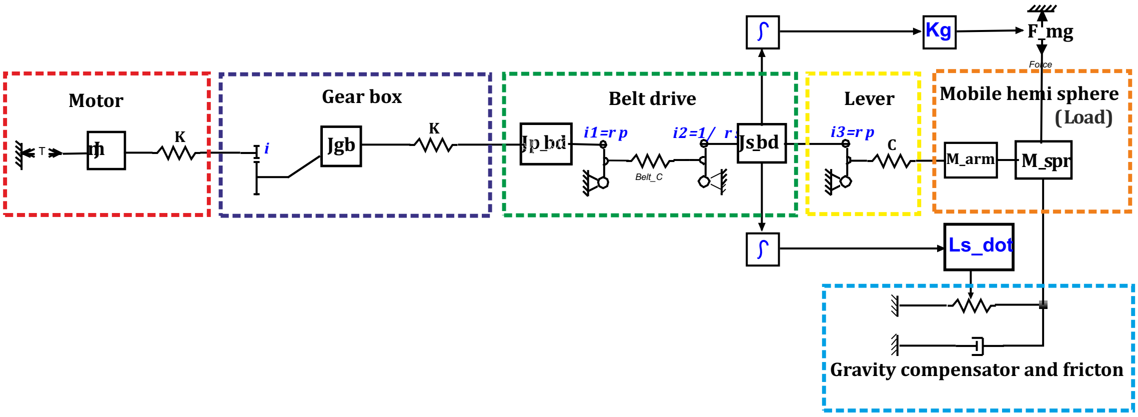

Figure 3.14: IPM for reconfiguration mechanism

Figure 3.14 shows the detailed IPM model for reconfiguration mechanism. Detailed IPM model of reconfiguration mechanism consists of torque applied by motor τ, motor inertia, gearbox inertia and ratio for motor gearbox, belt drive mechanism, lever and mass of mobile sphere (M_{sphr})as end effector. Secondary inertia of the belt drive is driving the mobile arm (flex arm). Moreover, the gravitational force (F_{mg}) acting on the mobile mass, gravity compensator and rolling friction is also considered in this system.

The stiffness of the timing belt is obtained from the manufacturing catalog, also the linear stiffness for gravity compensator is already known as 1800 N/m. The rolling friction value is 3.2(referring to (Naves (2014)). This friction required to transmit the power also affects the system's performance.

3.4.2 Model reduction and simplification of the reconfiguration mechanism IPM

IPM model obtained in Figure 3.14 is already reduced and relatively simple which gives the detailed understanding of dynamics of the reconfiguration mechanism. Although, further reduction and simplification is possible and done to obtain the flexible mechanism of reconfiguration mechanism. The flexible mechanism is one of the class of electro-mechanical motion systems which describes the dynamics of the system based on meaningful elements only (de Vries, 2014). Similar to the drive-train mechanism reduction and simplification, the reconfiguration mechanism in Figure 3.14 is reduced and simplified considering only significant inertias and stiffness of timing belt.

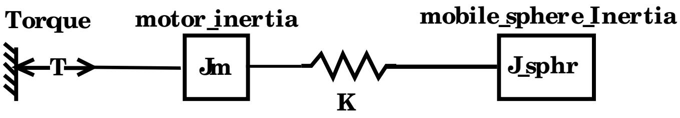

Figure 3.15: Reduced IPM for reconfiguration mechanism

The importance of reconfiguration mechanism can be defined for the control purpose as this mechanism limits the bandwidth of the DH-CVT. In addition to that, reconfiguration mechanism is developed to control the transmission ratio of the DH-CVT, which leads to further control of torque and position of the load. The working of the DH-CVT is highly dependent on the ratio controller developed for the reconfiguration mechanism.

The mechanism shown in the above Figure 3.15 is used to design the feed-forward in combination with the feedback PID controller i.e a ratio controller for the plant. Such a ratio controller is already developed (see the work in (Bonilla, 2016)). This ratio controller is briefly explained in section 2.2.4 and used in this work to demonstrate the Inertia Driven CPA experiment.

4 Controller design and simulations

The control of the device is built in three control layers, given as: position control, ratio control and torque control. In this work, the position control is referred to as the servo control. The servo and ratio controllers control the position of the load and the position of the reconfiguration mechanism, respectively. The ratio controller was priorly developed using the PID controller and used for simulation purposes, it is briefly mentioned in Section 2.2.4. For more details refer to (Bonilla, 2016). However, the design procedure for the servo controller is discussed in details in this chapter. Moreover, the torque control layer referred to as the abstraction layer implemented to generate the ratio setpoint of the CVT is explained beforehand. In the final sections of this chapter, the complete DH-CVT system simulations are performed in order to gain insight on the design of the inertia driven CPA experiment. The feasibility of the flywheel design is also confirmed by analyzing the simulation results.

4.1 Dynamics of the Inertia driven CPA : Abstraction layer

In order to control the state of the load by controlled energy transfer from the flywheel inertia ($I_{flywheel}$) to the load inertia (I_{load}), the desired transmission ratio is generated from the dynamics of the Inertia Driven system. Thus, a differential equation, Equation 4.1, is derived to describe the dynamics from the simplified bond-graph model as shown in Figure 4.1.

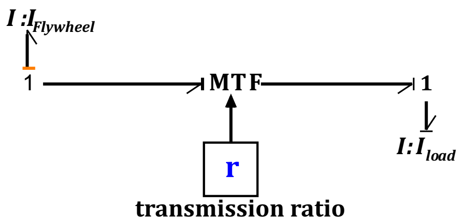

Figure 4.1: Bond graph of Inertia Driven CPA

$$\ddot{\phi}_{load} = \frac{\frac{1}{r^3}\frac{I_{flywheel}}{I_{load}}\dot{r}\dot{\phi}_{load}}{1+\frac{1}{r^2}\frac{I_{flywheel}}{I_{load}}} \tag{4.1}$$

Since the system dynamics are non-linear, an abstraction layer is created by partially inverting the dynamics of the system. It is created to abstract the inertia-driven Controlled Passive Actuation to a torque actuator. Feedback control can be applied on the abstracted system to achieve control goals such as path tracking. $\dot{r}$ is calculated as:

$$\dot{r} = \frac{\tau_{ad}(r^2 + \frac{I_{flywheel}}{I_{load}}}{I_{flywheel}}\dot{\phi}_{flywheel} \tag{4.2}$$

Where $\dot{r}$ is the mobile sphere velocity, τ_{ad} the desired actuation torque to the DH-CVT, r the transmission ratio of the DH-CVT, $I_{flywheel}$ the inertia of the flywheel, $\dot{\phi}_{flywheel}$ is the flywheel velocity and I_{load} the inertia of the load.

The selected motion profile is the most commonly used second order motion profile, a trapezoidal position profile. The selected trapezoidal position motion profile is given as a reference signal to track the actual load position. The tracking error between reference and actual position can be observed. This specific motion profile is shown in Figure 4.5.

4.2 Controller design

A PD controller is developed to achieve the servo motion of the system by controlling the damped second order behavior of the position. It adds phase lead, improves phase margin, improves damping, resulting in a minimized resonance condition, and thus improves the performance of the system. The abstraction layer (torque control layer) created in Equation 4.2, can be treated as linear, making the design of the controller straight forward.

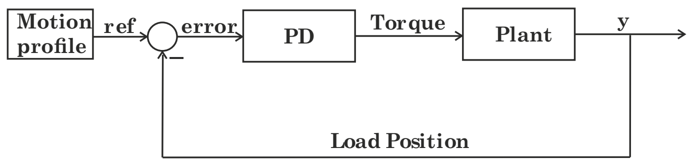

Figure 4.2: Servo control structure

4.3 Simplification of the plant for the controller design

Referring to (de Vries, 2014) and (Coelingh, 2000), to design the servo controller for the DH-CVT IPM the model can be further reduced to one of the classes of the electro-mechanical motion system. *'An electro-mechanical motion system is an electrically actuated plant that requires to control the position of an end effector (load)'.* It describes the dynamics of the system based only on the meaningful elements. Then, by combining all the inertias, except the load inertia, as one inertia (I_{system}), and considering the load inertia (I_{load}) as other inertia separated by a very stiff spring, the highly non-linear reduced model shown in Figures 3.6 and 4.3 is approximately linearized to a flexible mechanism class of the electro-mechanical motion system. This model is useful for designing the servo controller for the DH-CVT. The reduced linear model is a fourth order plant, shown in Figure 4.4,

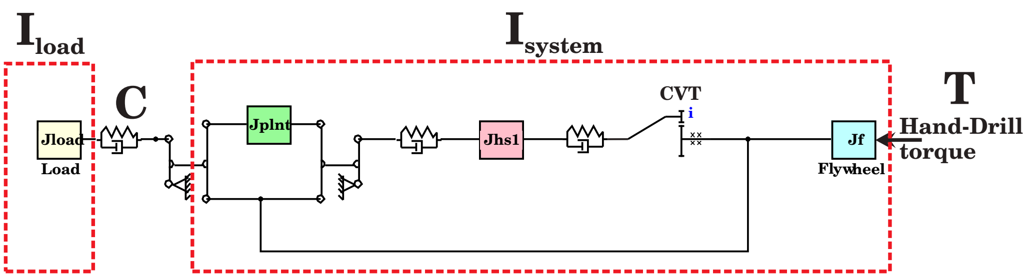

Figure 4.3: Approximate simplification of the non-linear to linear model for control purposes

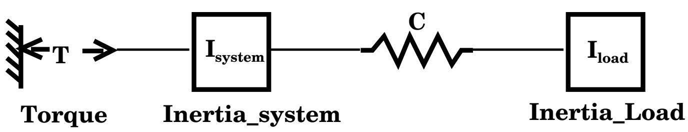

Figure 4.4: Reduced fourth order model (Flexible Mechanism)

An Inertia-spring-Inertia system with applied torque as depicted in Figure 4.4, indicates a common fourth order model. *'The fourth order model is a lumped parameter representation of the dominant dynamic behavior of the electro-mechanical motion systems in which only rigid body mode and lowest mode of vibration are taken into account' (Coelingh, 2000).*

I_{system} = Total inertia of the drive-train model = $1.75 \times 10^{-3} Kg \cdot m^2/rad$
I_{load} = Inertia of the load = $6.3 \times 10^{-4} Kg \cdot m^2/rad$
C = connecting stiffness = $10^5 N \cdot m/rad$

Flexible mechanisms can be of type AR (Anti-resonance) or R (Resonance) depending on whether the feedback position is measured in the system's inertia, I_{system}, or in the load's inertia, I_{load}, respectively. The feedback angular position of the load is then measured at the load's inertia I_{load}, and hence the transfer function is of R type.

The parameters for an R type transfer function are: (de Vries, 2014)

$$m = m_1 + m_2 \tag{4.3}$$

$$\omega_{ar} = \sqrt{\frac{c}{m_1}} \tag{4.4}$$

$$\omega_r = \sqrt{\frac{c(m_1 + m_2)}{m_1 \cdot m_2}} \tag{4.5}$$

To calculate the cross-over frequency ω_c required for a stable controller, the maximum acceleration needs to be calculated from the selected motion profile. The following figure shows the second order motion profile and indicates the parameters required for calculating the maximum acceleration.

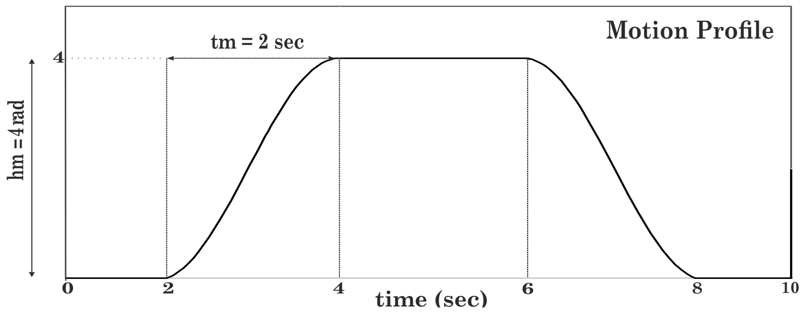

Figure 4.5: Second order motion profile

In the motion profile, the desired load position is chosen as $h_m = 4rad$ in a stroke in time $t_m = 2sec$. Thus, the required maximum acceleration and controller cross over frequency can be calculated as:

$$\ddot{X}_{max} = \frac{4 \times h_m}{t_m} = \frac{4 \times 4}{2} = 8 \ \ \text{rad/sec}^2 \tag{4.6}$$

The cross-over frequency can be calculated as:

$$\omega_c = \sqrt{\frac{\ddot{X}_{max} \times \sqrt{\beta}}{e_{max,track}}} \rightarrow \omega_c = \sqrt{\frac{8 \times \sqrt{10}}{0.00005}} = 224.9 \ \ \text{rad/sec} \tag{4.7}$$

Where, h_m = Desired angular position (stroke), t_m = time required for one stroke, β = derivative gain limitation = 10,
$e_{max,track}$ = maximum tracking error considered = $0.5mrad$

From Equation 4.5, the resonance frequency is $\omega_r = 14692.6\ rad/sec$, which is very high compared to the cross-over frequency $\omega_c = 224.9 rad/sec$ as the connecting stiffness is very high ($10^5 N.m/rad$) compared to the total and load inertias. According to the stability analysis condition, $\omega_r > 4 \times \omega_c$ for the transfer function type R. Hence the system is stable (de Vries, 2014).

The connection's stiffness between the two inertias is of very high value and can be considered as a rigid connection. Therefore the system can be considered as a single moving inertia.

$$I_{total} = I_{system} + I_{load} = 2.38 \times 10^{-3} Kg.m^2/rad \tag{4.8}$$

The simple transfer function for the plant can be written as,

$$P(s) = \frac{1}{I_{total} s^2} = \frac{1}{0.00238 s^2} \tag{4.9}$$

The plant described in the above equation is used for the design of the PD controller to achieve the servo control for the DH-CVT system.

For the linearized plant, it is possible to calculate the tuning parameters by using the rules of thumb for the PD controller. However, it is known that the DH-CVT system is highly non-linear and approximately linearized to initialize the controller's design process properly. Hence, it is expected that the designed controller with the tuning parameters obtained from the rules of thumb might not provide a satisfactory performance. This performance is evaluated in the next section. If the performance of the PD controller is not adequate, an unconventional design process for the design of the modified PD controller to obtain the desired system performance can be used.

4.4 PD controller design using rules of thumb

Considering the total inertia (I_{total}) as an ideal plant, the calculated cross-over frequency ($\omega_c = 224.9 rad/sec$) and the derivative gain limitation ($\beta = 10$), the following tuned parameters are obtained for the controller design.

$$K_p = \frac{\omega_c^2 I_{total}}{\sqrt{\beta}} = \frac{224.9^2 \times 0.00238}{\sqrt{10}} = 38.06 \tag{4.10}$$

$$\tau_z = \sqrt{\beta}\frac{1}{\omega_c} = \sqrt{10}\frac{1}{224.9} = 0.0141 \tag{4.11}$$

$$\tau_p = \frac{\tau_z}{\beta} = 0.00141 \tag{4.12}$$

The transfer function of the PD controller can be written as:

$$C(s) = K_p[\frac{1 + s\tau_z}{1 + s\tau_p}] = \frac{38.06 + 0.5366 * s}{1 + 0.00141 * s} \tag{4.13}$$

The performance of the PD controller is identified in Figure 4.6.

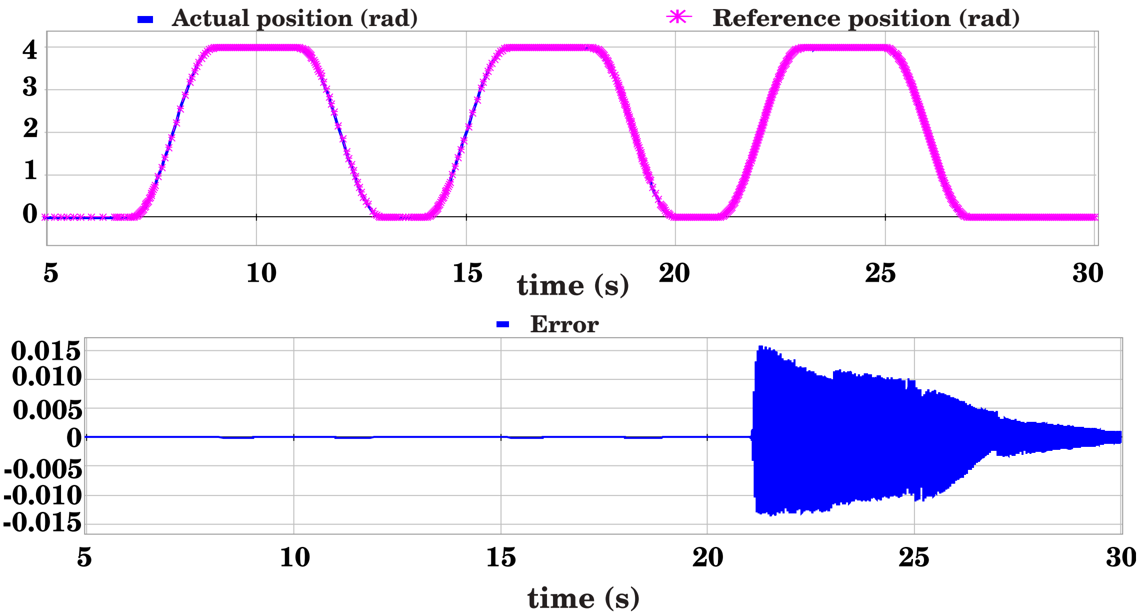

Figure 4.6: Noise in the performance of the system

The above figure clearly shows that the load closely tracks the reference profile and thus the tracking performance provided by the PD controller is satisfactory. However, measurement noise can be observed at high frequencies, which affects the system's performance. Additionally, Figure 4.6 depicts noise observed after 21 seconds of the simulation, which might be due to the limited accuracy of the integration method of the simulator. Indeed, during the simulation, it is observed that the noise content in the performance varies according to the change in the accuracy of the integration method used for the simulation. However, the noise never goes away completely. Hence, noise reduction by proper control is necessary.

There are two disturbances acting on the plant, the load disturbance and the measurement noise. Load frequencies are dominated by low frequencies, while noise is a high frequency behavior. The control is based on the measured load position and this measurement can be corrupted by the measurement noise in the system. Measurement noise is injected into the system by feedback. This is unavoidable but essential to ensure that the injected noise does not affect the system's performance significantly (Astrom, 2002).

Load disturbances drive the load away from its desired behavior. From Figure 4.6, the load disturbances are almost nullified and the load is tracking the desired path (*the tracking error corresponds to 0.004 $mrad$ before 21 seconds* 4.6). After 21 seconds, it is observed that the noise still does not affect the load's tracking considerably. The load is vibrating due to the high frequency noise and the tracking error is increased to 0.015 rad (*visible in figure 4.6 after 21 seconds*). This is due to the fact that when the controller has high gain the measurement noise is amplified as well, and fed into the system. Subsequently, a new approach is followed to design a new controller in order to obtain the desired path tracking and attenuated noise performance.

4.5 Modified PD controller design

In order to reduce the noise, the controller's proportional gain (k_p) is reduced, while the derivative gain limitation (β) is increased. The increased derivative gain limitation magnitude increases the filtering effect (Astrom, 2002). Despite the fact that the tuning required in this approach is by trial and error, it is implemented since it provides the desired path tracking and noise attenuated response. The tuning procedure is explained next.

The modified tuning parameters are $K_p = 9$, $\tau_z = 0.0141$ and derivative gain limitation $\beta = 15$. The transfer function is given as:

$$C(s) = K_p[\frac{1 + s\tau_z}{1 + (s\tau_p)}] = \frac{9 + 0.1269 * s}{1 + 0.00094 * s} \tag{4.14}$$

The change in the controller behavior is seen in Figure 4.7. It is observed that decreasing the proportional gain decreases the gain's magnitude in the low frequency region. Consequently, decreasing the injected noise in the system. The trade off between the decrease in the proportional gain and the increase in the derivative gain limitation (β) increases the phase, which in turn increases the damping. Therefore, it is expected to see the noise attenuated response. The following figure compares the original and modified PD controller in the frequency domain.

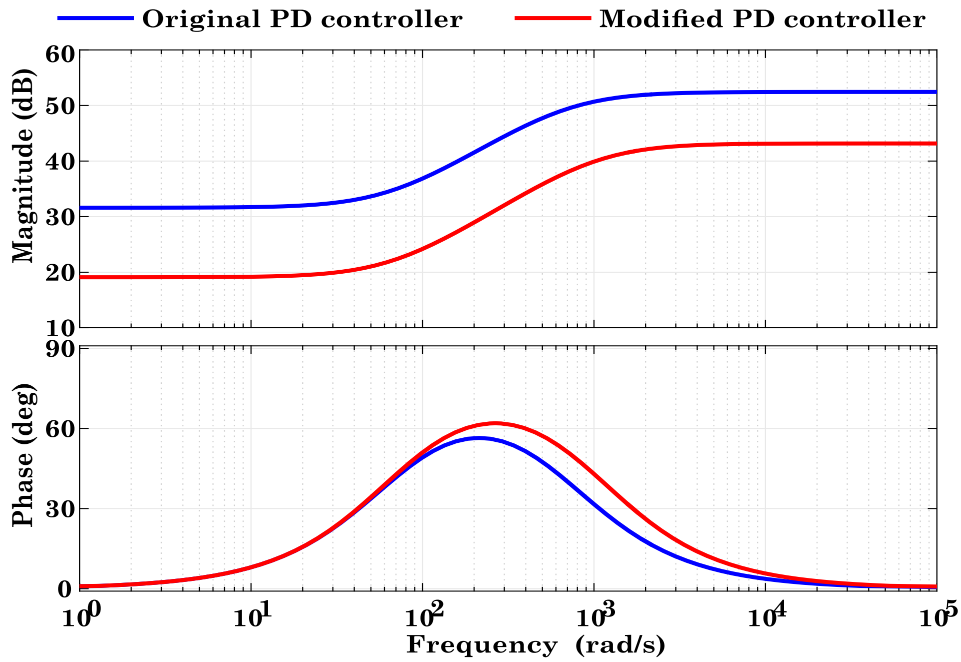

Figure 4.7: Change in the controller behavior

Next, the performance of the system with a modified PD controller is evaluated.

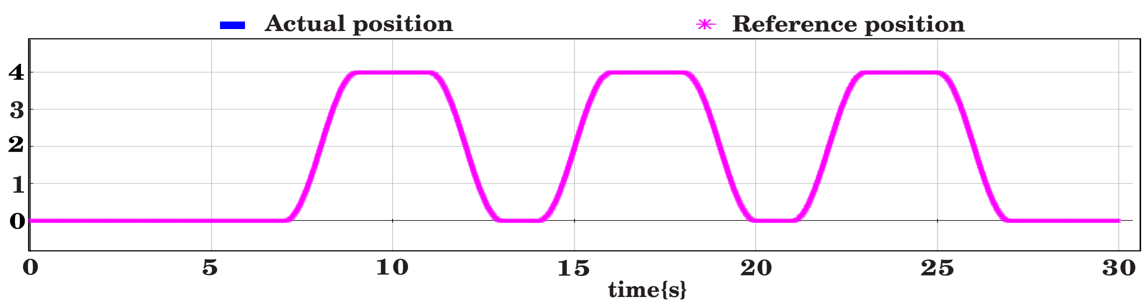

Figure 4.8: Load position tracking

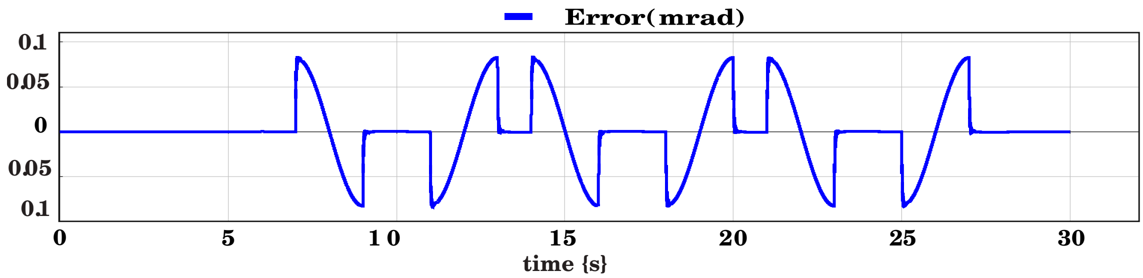

Figure 4.9: Tracking Error: Noise attenuated response

The path tracking and error plot shown in Figures 4.8 and 4.9, respectively, illustrate that the desired path tracking with better noise rejection is obtained with the modified PD controller rather than with the original PD controller - Figure 4.6. The stability analysis for both of the controllers is done in next section.

4.6 Comparison of the original and modified PD controller: stability and response

The bode diagram plotted in Figure 4.10 showed that the cross-over frequency of the modified PD controller is $75 rad/sec$, lower than the cross-over frequency of the original PD controller, $225 rad/sec$. This indicates that the modified PD controller is slower than the original PD controller. Moreover, the gain margin for both controllers is infinite and the phase margin is positive i.e 44.59 deg for the modified and 55.23 deg for the original controllers. Hence, both of the controllers are closed loop stable. It can also be observed that the modified PD controller is slower than the original PD controller, but that is the very small price to pay in order to obtain the noise free response.

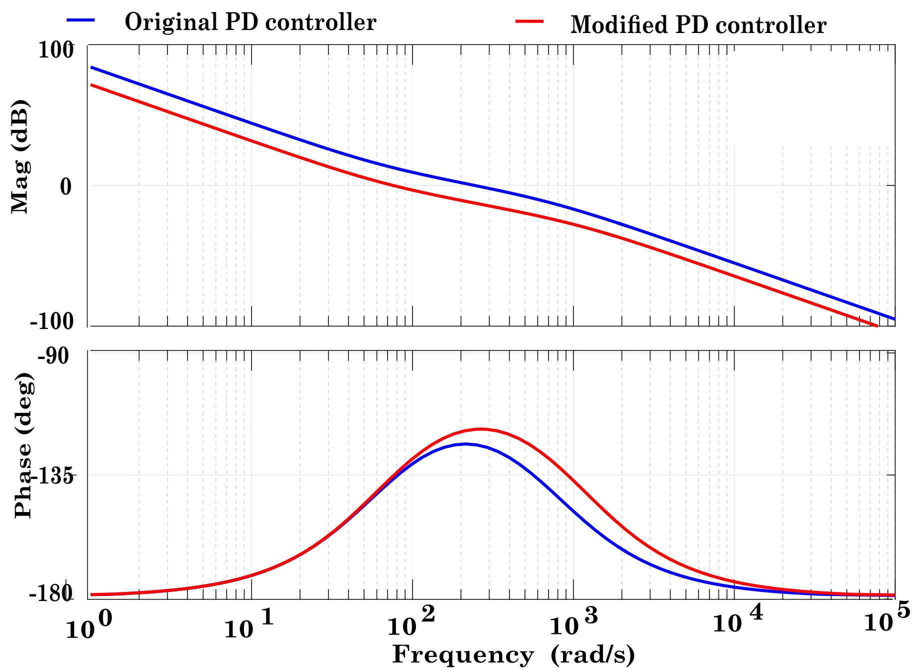

Figure 4.10: Closed loop response - Bode plot

Similar to the frequency domain analysis done with the bode plot in Figure 4.10, the Nichols plot also depicts the closed loop stability. It also showed that both controllers have stable behavior, since both of their behavior are further away from the unstable region known to be around 6dB region.

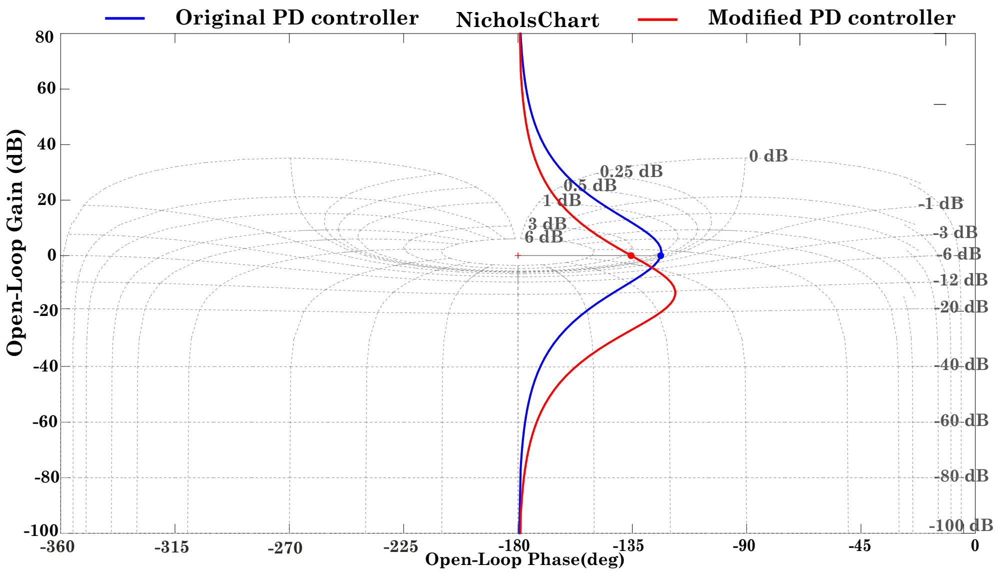

Figure 4.11: Nichols plot for second order plant

Stable controller behavior and better simulation performance are obtained with the use of the modified PD controller, the complete Inertia driven DH-CVT system simulation are carried out using the modified PD controller in the next section.

4.7 Simulation approach and results

The following simulation are conducted to gain good understanding of the desired load motion and the controlled energy flow through the system. Satisfactory simulation result would assist in the design of the inertia driven CPA experiment.

Note:

The simulation results obtained in Section 4.7 provide acceptable insight for the design of the inertia driven CPA experiment. The experiments are conducted based on the results mentioned in Section 4.7. However, the experimental results pointed out that actual friction in the system is more than what is considered in the current simulations. The friction model is misplaced from it's correct location. A revised simulation is therefore presented. Refer to Section 4.8 for revised simulation results.

• *Owing to the time limitation, the use of the misplaced friction in the model was an instrumental decision taken to pursue with the progress of the assignment.*

4.7.1 Simulation model:

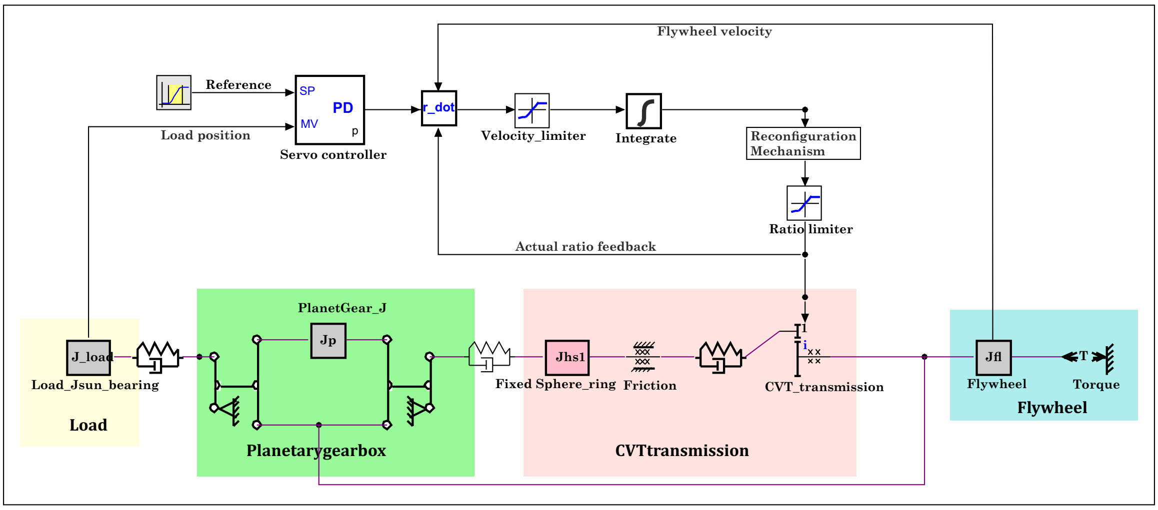

Figure 4.12: Simulation model in `20-sim`

Figure 4.12 depicts the simulation model developed in `20-sim`. The torque control is achieved by using the dynamics of the inertia driven system, as explained in Section 4.1. A servo controller (modified PD controller) is used to control the load position. Moreover, the ratio controller is implemented in the reconfiguration block (*not depicted*). To understand the simulation model better, some important points are discussed below.

In Section 4.1, $\dot{r}$ is the mobile sphere velocity (i.e the rate of change of the transmission ratio) which is calculated to generate the desired ratio required for achieving the targeted load motion. Yet, there is a certain limit for the rate of change of the transmission ratio for generating the desired ratio within the ratio range.

There is a certain contact friction force required between the two hemi-spheres in order to prevent the slip / failure of the CVT to ensure the efficient energy transfer through the system (Dresscher et al., 2016). This means that there is a certain velocity range for the mobile sphere to maintain that contact friction force and generate the transmission ratio within the limit. If the velocity of the mobile sphere goes out of that particular limit, slip might occur between the two hemisphere causing tremendous increase in friction, resulting into sudden energy loss and the load's abrupt ceased movement. Thus, a velocity limiter is placed in series with the r_{dot} block to keep the $\dot{r}$ within limit. The actuation torque τ_{ad} is generated such that $\int \dot{r}$ stays within the boundaries of r. Analytically, the transmission ratio is calculated as:

$$\text{transmission ratio} = \frac{\text{Load velocity}}{\text{Flywheel velocity}} \tag{4.15}$$

Such that the transmission ratio is always related to the source velocity and the load velocity. The flywheel velocity should never go to zero, otherwise there will be no actuation torque. Therefore, r will go to zero when load velocity goes to zero. If the integral of $\dot{r}$ stays within the boundaries of r, then inertia driven CPA can be applied.

In Figure 4.12, the whole PS-CVT simulation model is created using three control layers. A Feed-forward PID controller is implemented for the reconfiguration mechanism generated the actual ratio by measuring the angular position of reconfiguration mechanism (*Feed-forward PID controller is shortly explained in Section 2.2.4 and the extensive work is done in (Bonilla, 2016)*). The actual ratio is fed back to the transmission as an input.

In the upcoming subsection, the results of the simulations for the Inertia driven CPA experiment for the friction-less system, which gave us insight of the performance of the inertia driven CPA in the ideal case, will be discussed (i.e. the loss less situation is investigated). Later, simulation results with friction in the system which gave a realistic performance of the system to design the inertia driven CPA experiment are investigated.

The necessary actions in the simulations are systematically performed into four different phases, given in table 4.1.

Phase	time in seconds
Ratio initialization	0 - 3
Zero transmission ratio	3 - 7
Flywheel energy storage phase	4 - 4.37
DH-CVT system motion phase	at 7 onward

Table 4.1: Inertia driven CPA: Simulation phases

Following the phases mentioned in Table 4.1, the simulations are conducted and the ratio initialization is done for the first 3 seconds. Then, the transmission ratio is made zero for the time interval of 3 to 7 seconds called as transmission ratio zero phase. This interval also contains the flywheel energy storage phase, since the flywheel should be accelerated at the transmission ratio zero to avoid unnecessary energy transmission in the system. It allows to store the energy in the flywheel efficiently. Once the required energy is stored in the flywheel, the DH-CVT system motion phase starts at 7 seconds. In this phase, the energy from the flywheel is transferred to the load in a controlled manner such that the desired load motion is achieved. The following results are attained.

4.7.2 Simulation results for a friction-less system

The load motion, ratio control and energy flow through the system are observed for the lossless system. The following results are obtained:

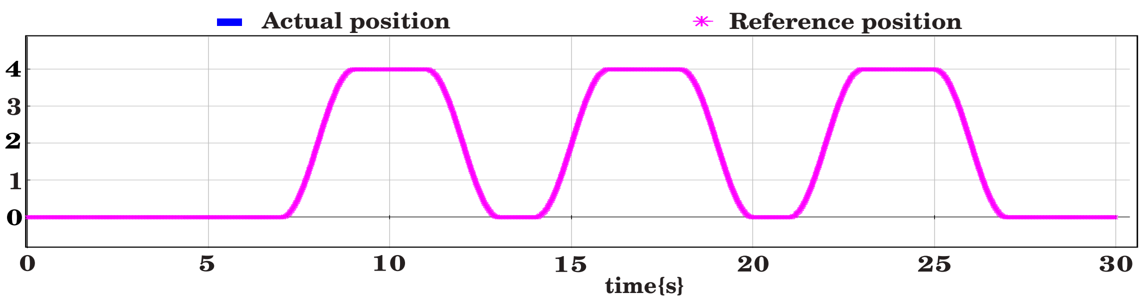

Figure 4.13: Load position tracking

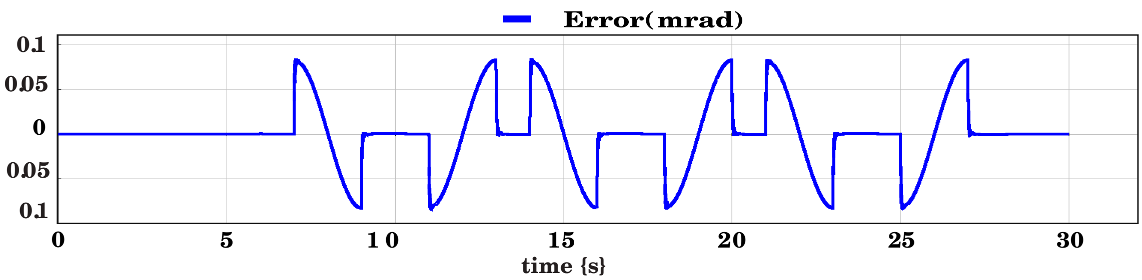

Figure 4.14: Load position tracking Error

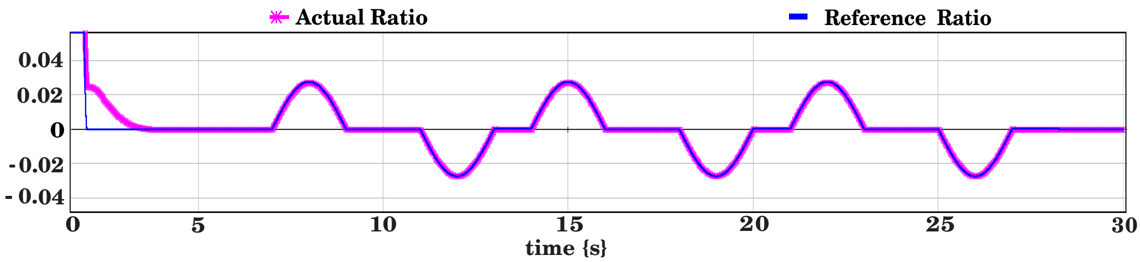

Figure 4.15: Transmission ratio

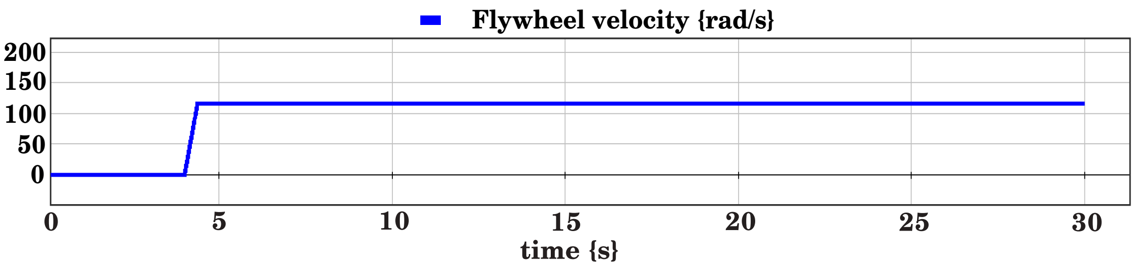

Figure 4.16: Flywheel velocity

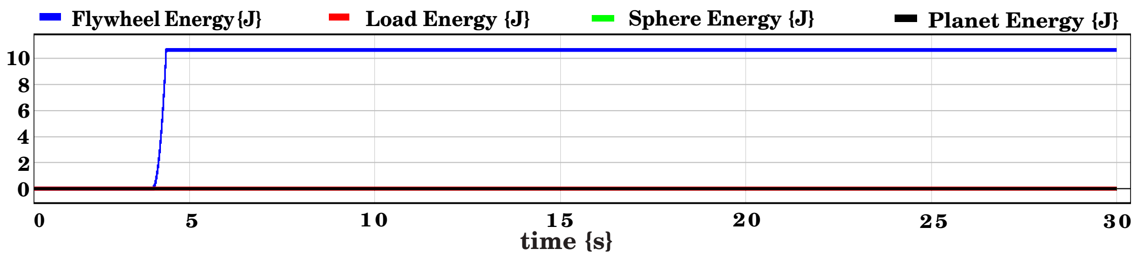

Figure 4.17: Energy flow through the friction-less system

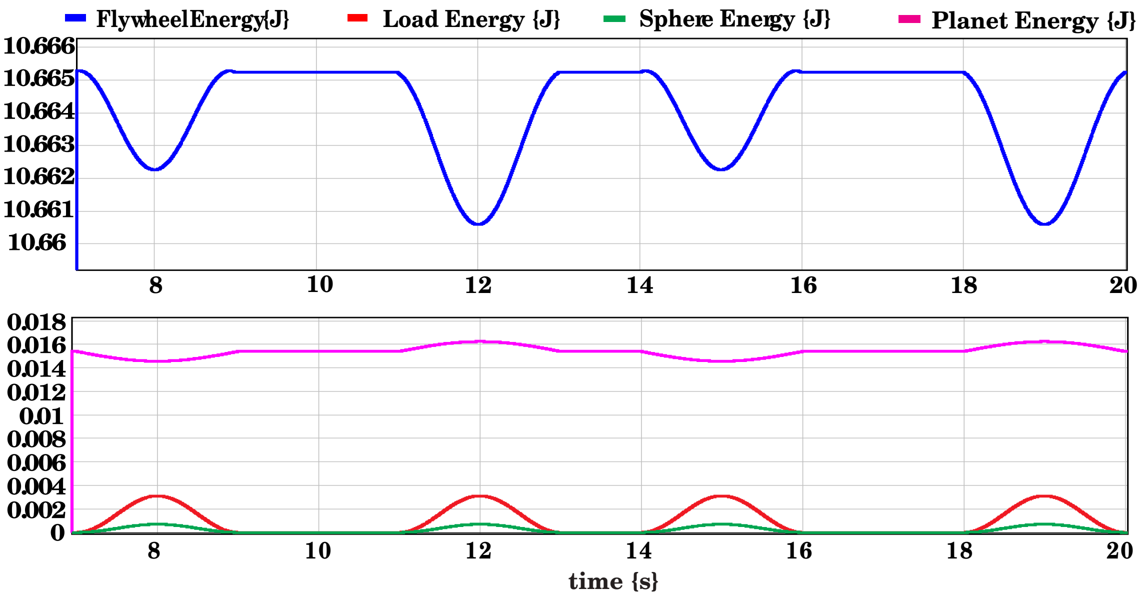

Figure 4.18: Detailed illustration of energy flow through the system

Figure 4.13 shows that the load position is tracking the reference position accurately, showing the desired behavior. Moreover, it is obvious to observe that load follows the perpetual motion, since it is a loss-less system. The tracking error is almost negligible, 0.08 $mrad$ as indicated in Figure 4.14.

From Figure 4.15, it can be observed that the controlled transmission ratio generated from the reconfiguration mechanism is tracking the reference transmission ratio. The magnitude of the transmission ratio is very low as the energy transfer required to drive the output load is of small value, shown in Figures 4.17 and 4.18. Additionally, the ratio is similar throughout the acceleration and deceleration of the load, as the flywheel velocity and load velocity are both constant.

Additionally, Figure 4.16 describes the flywheel rotation up to 350 rpm i.e. $\approx$ 36 rad /sec velocity (visible as reduced flywheel velocity in the simulation model = 116 rad/sec). In order to store the kinetic energy in the flywheel, the flywheel is accelerated by the actuation torque obtained from the hand-drill. (*NOTE: An hand-drill was chosen to accelerate the flywheel since it was the cheapest and most accessible option.*) In Figure 4.16, the flywheel velocity trajectory is continuously increasing for a short amount of time so that it reaches the desired level of velocity ($\approx 116 rad/sec$) and then remains constantly rotating at the same velocity - considering losses due to friction are neglected in this simulation. Thus, the energy stored in the flywheel remains constant at 10.42 J - Figure 4.17. This allows the load to exhibit continuous motion. Moreover, it is be observed from Figures 4.15 and 4.16 that the energy is stored in the flywheel by rotating it when, the transmission ratio is zero. The flywheel is rotated at the transmission ratio zero.

Figures 4.17 and 4.18 indicate the very low consumption of energy for the load motion. Figure 4.18 interpret the detailed energy flow analysis. Similar to the flywheel inertia, it is also important to consider that the planetary gear inertia is coupled to the same shaft connecting the flywheel, leading to little amount of energy stored in the planet inertia. The observable peaks in the stored flywheel energy plot describes the energy consumption in order to drive the system. During the acceleration of the output load disc, the system uses the energy mostly from the flywheel energy storage and a small amount of energy from the energy stored in the planet inertia - see energy flow at time = 8 sec in Figure 4.18. However, during the deceleration, the planetary gear absorbs little amount energy from the flywheel allowing the output load disc to move in the opposite direction. In addition to that, the load used the energy from the flywheel energy storage and hence, it can be clearly observed that the energy consumption is more than the previous case - Figure 4.18 at 12 sec. It is essential to mention that, the energy consumption to drive the load is very low since the acceleration of the output load disc is relatively low.

4.7.3 Simulation results considering friction in the system

The following results are obtained considering the dynamic friction behavior in the system. In this simulation, the ideal friction model is used, showing the same friction torque as the actual friction model. It is used because the simulation with the actual friction model causes time switches, making it hard for the simulator to process the data - refer to Section 3.3.3. These simulation results are expected to be realistic and give good insight for the actual experiment. The energy loss due to friction and energy flow through the system were then observed - Figure 4.24.

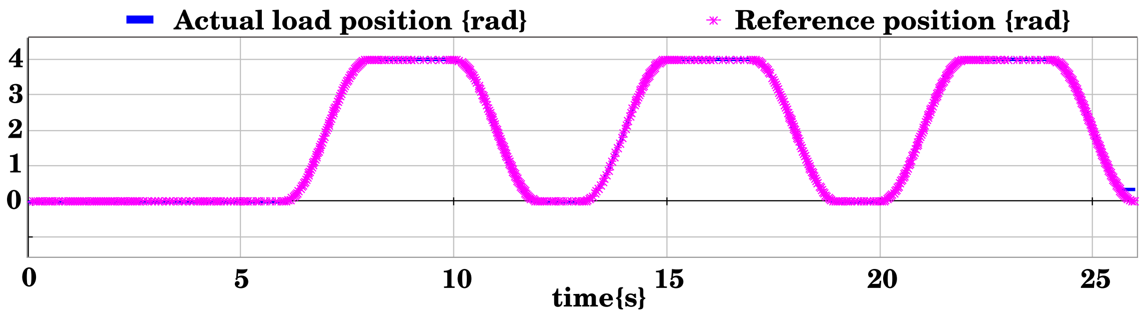

Figure 4.19: Load position tracking

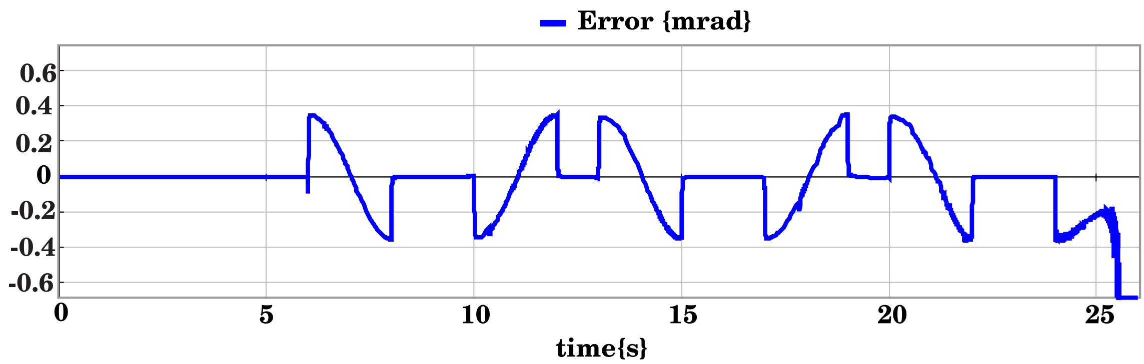

Figure 4.20: Tracking error

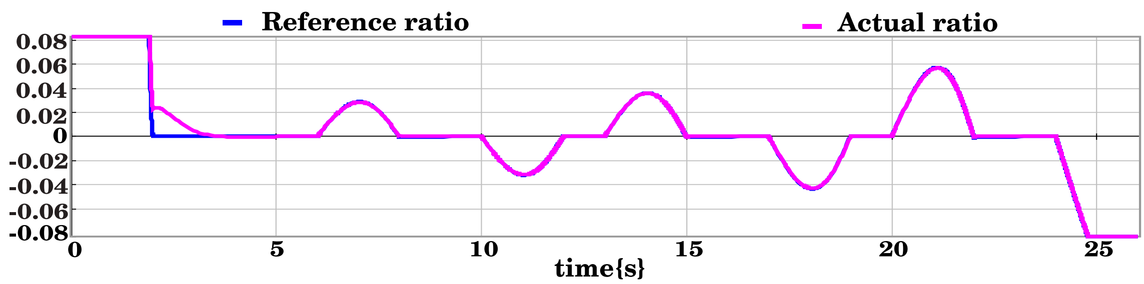

Figure 4.21: Transmission ratio

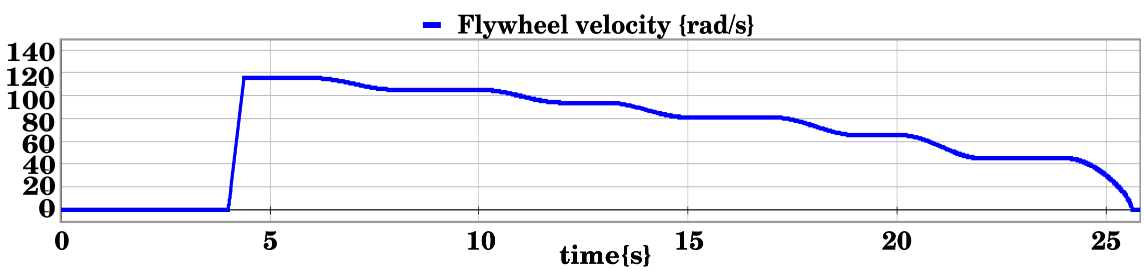

Figure 4.22: Flywheel velocity

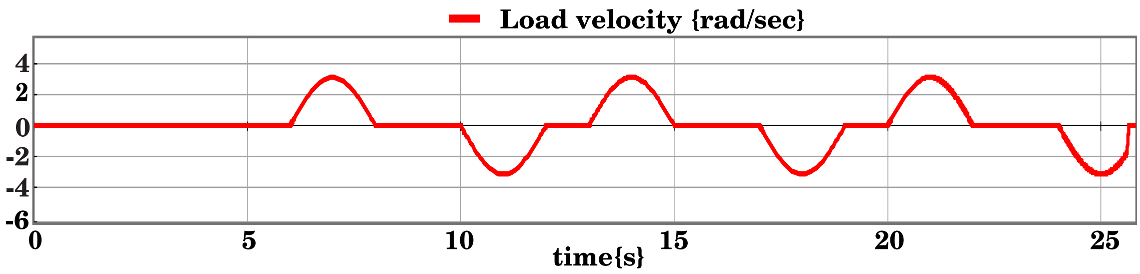

Figure 4.23: Load velocity

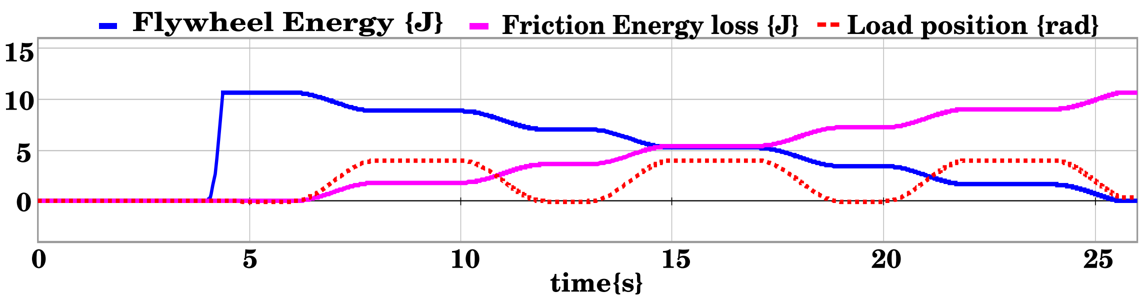

Figure 4.24: Flywheel energy and friction energy loss

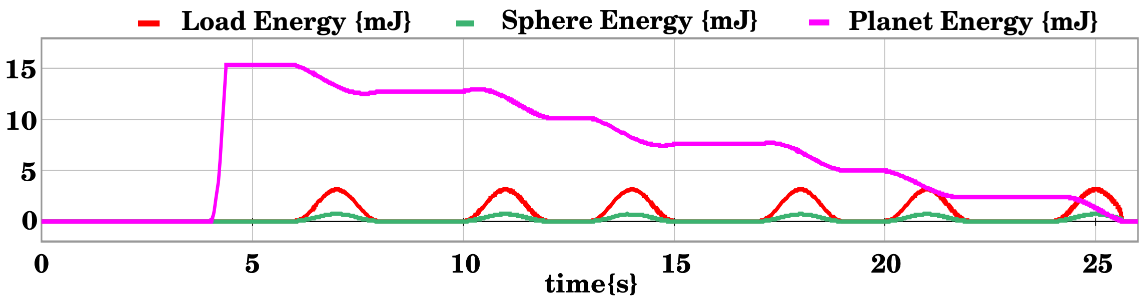

Figure 4.25: Energy flow through the system

As mentioned in Table 4.1, from Figure 4.21 the ratio initialization is done for the first 3 seconds. Then, the transmission ratio is made zero for the period of 3-6 seconds. This period also includes the flywheel rotation phase for 4 to 4.37 seconds.

The flywheel is rotated at the transmission ratio zero to avoid unnecessary energy transmission from flywheel to load. The load is stand-still during the zero transmission ratio as shown in Figure 4.20. In this period, the flywheel is sped up to 350 rpm (*visible as a reduced flywheel velocity* $= 116\ rad/sec$) i.e. the required energy ($10.42J$) was stored in the flywheel, see Figure 4.22.

Once the flywheel was rotated to the desired speed, the system motion phase started at 6 seconds. In this phase, the energy is transferred to the load in a controlled way in order to achieve the desired load position (see Figure 4.20) by controlling the ratio with the help of the ratio controller. It can be observed in Figure 4.21 that the ratio is changed - being positive during the acceleration and negative during the deceleration of the load. Obviously, the transmission ratio required is low in magnitude, since the energy required to transfer to the load is relatively low - Figure 4.25. Moreover, it can also be observed that the ratio is increasing over the period to keep the load velocity of same value, since the energy stored in the flywheel is decreasing gradually, as depicted in Figure 4.23.

Not to mention, the servo controller (modified PD controller) provided the desired actuation torque by controlling the load position. The desired load motion is observed for almost until 25 seconds. The desired load motion and very low tracking error (Figure 4.20 $\approx$ 0.3 $mrad$) suggested that the servo controller (modified PD controller) provided acceptable performance and can be tested in the inertia driven CPA experiment.

The friction considered in the simulation provided the friction loss during the system motion phase only, seen in Figure 4.24. Nevertheless, there might be some additional frictional effects that can be seen during the flywheel rotation phase, which might lead to unexpected results during the experiment. Hence, it is important to pay extra attention to the internal friction acting on the system during the experiment. The energy flow in the system showed that the energy is dissipated gradually and converted into heat due to the friction, eventually.

Additionally, the energy flow in the other parts of the system can also be observed - Figure 4.25. Since, the planetary gear is directly coupled to the flywheel, it also stored a small amount of energy. However, in this case, the stored amount of energy in the planetary gear is more that the dissipated load energy. This is due to the fact that the acceleration of the load is very low and requires relatively small amount of energy for its motion. Moreover, the energy dissipated by the fixed hemi sphere for the motion is also very small, since the inertia of the fixed hemi sphere is very low.

Collectively, these simulation results implied that the Inertia driven CPA can be applied as a source of effort for the actuation when using the DH-CVT. As mentioned, it would be interesting to see the effect of the actual internal friction in the system during the experiment. Not to mention, they also implied that the designed flywheel model in section 3.3 is sufficient to obtain desired results. Hence, the flywheel model can be manufactured and integrated in the DH-CVT system.

The inertia driven experiment is designed based on the insight gained from the aforementioned simulation results. The experiments and findings are explained in the next chapter.

4.8 Revised simulation

A detailed explanation concerning the realistic friction effect, observed during the experiment, is given at the end of Section 5.3.1 of Chapter 5. In this section, Section 4.8, only revised simulation results are mentioned.

Results and analysis

A new insight is gained for the friction behavior in the system from the experimental results. Therefore, the friction model is placed at the correct location and revised simulations are performed using the actual friction model mentioned in Figure 3.12.
It is expected that the revised simulation model should show a more realistic effect if the friction model is placed at the input of the system, between the CVT transmission and the flywheel. Next, the elaborated results considering the correct friction location are shown as follow:

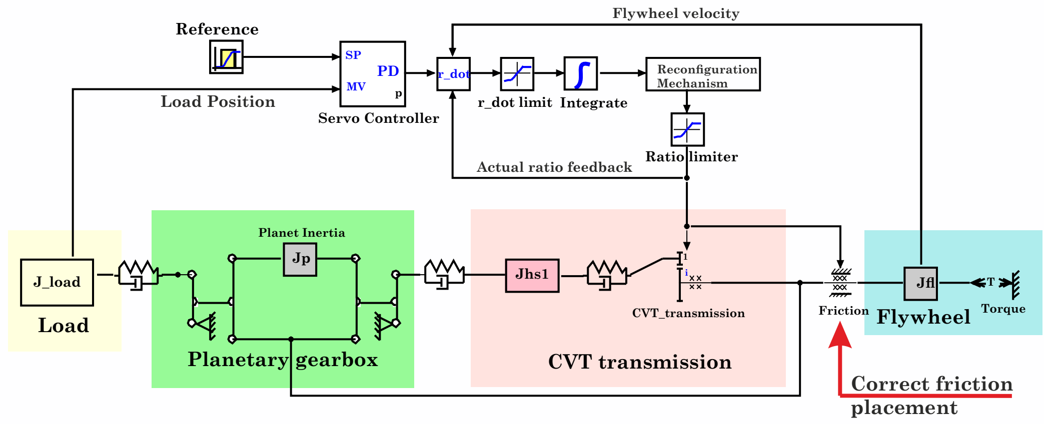

Figure 4.26: Revised simulation model

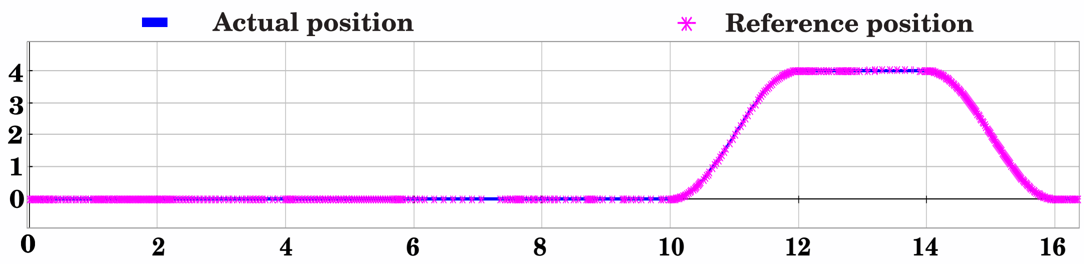

Figure 4.27: Revised simulation: Load tracking

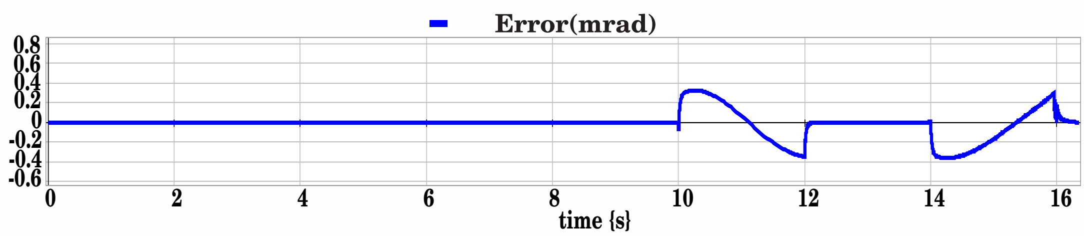

Figure 4.28: Revised simulation: tracking error

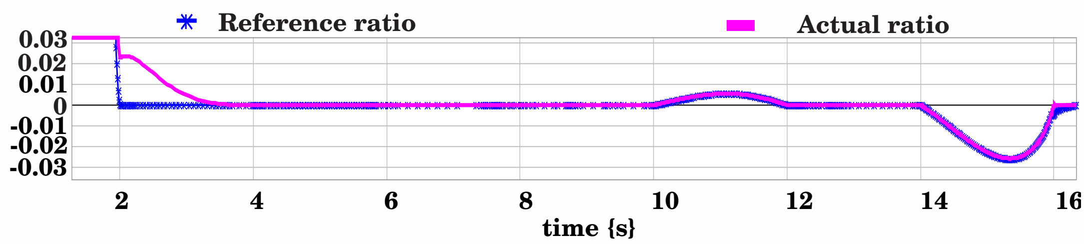

Figure 4.29: Revised simulation: Ratio tracking

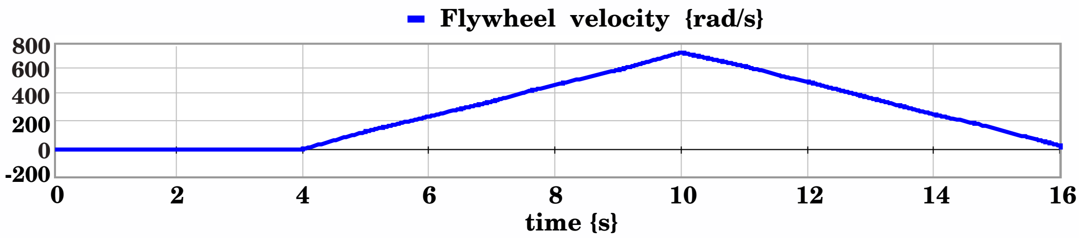

Figure 4.30: Revised simulation: Flywheel velocity

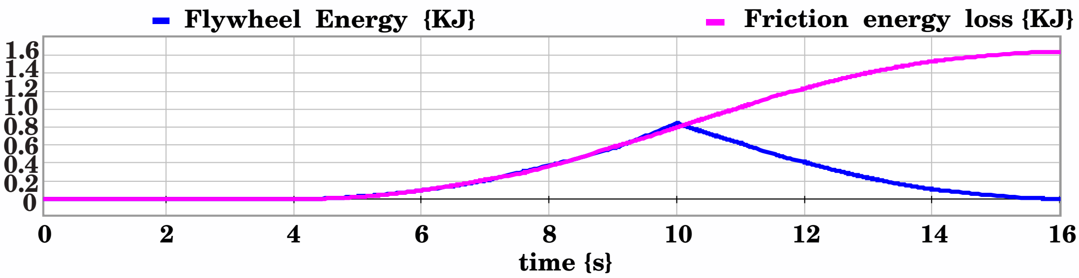

Figure 4.31: Revised simulation: Energy flow

The friction's placement accounts for the friction during the flywheel's energy storage phase and when the system is in motion, see Figure 4.31. This is because the friction is placed before the transmission i.e. it recognizes the energy at the input part of the system independent of the transmission. This effect is realized during the experiment by observing and noticing other parts of the system are rotating with the flywheel during the energy storage phase. Increase in the friction loss surely increased the requirement of the energy in the system. Thus, to increase the energy content in the system, the flywheel with increased inertia is rotated with high velocity. Figure 4.30 shows the flywheel velocity plot. The flywheel's kinetic (co)energy is calculated in the equation below.

$$E_f = \frac{1}{2} I_f \omega_f^2 = \frac{1}{2} 0.041 \times (1976 \times \frac{\pi}{30})^2 = 882J \tag{4.16}$$

This much flywheel energy content provides almost 16 seconds of load motion, sufficient for the inertia driven CPA experiment to be concluded. Following Table 4.2 indicates the newly estimated flywheel parameters for the inertia driven CPA experiment.

Actual flywheel velocity	1976 rpm ($\approx$ 207 rad/sec)
Actual flywheel inertia	0.041 $Kg.m^2/rad$
Reduced flywheel velocity	700 rad/sec
Reduced flywheel inertia	0.0036 $Kg.m^2/rad$

Table 4.2: New flywheel parameters for Inertia Driven CPA

The subsequent reduced flywheel inertia and velocity parameters that are used in the simulations are also mentioned in Table 4.2. Proper path tracking in Figure 4.27, low tracking error in Figure 4.29 and good ratio tracking in Figure 4.29 illustrate that the same modified PD controller used in the previous simulations (see Section 4.7) gives acceptable performance for revised simulations as well. Nevertheless, using the same material (brass) and same mechanical design equations that are used in Section 3.3.2, the flywheel's mass was calculated to be 4.12 Kg - provided the geometrical dimensions of the flywheel. In this scenario, the amount of energy that needs to be stored in the flywheel results in an unrealistic parameter for the velocity and inertia for the designed DH-CVT system, and hence cannot be implemented in practice.

5 Experiments and findings

This chapter thoroughly describes the experiments conducted and subsequent results. Firstly, the experimental setup is presented. Next, the experimental procedure and demonstration results of the Inertia driven CPA method are provided. Then, further experiments are performed to deepen the insight in the phenomena that showed up in these results. The different experiments and the steps taken in each experiment are given. Lastly, the results of the aforementioned are presented and discussed.

5.1 Experimental setup

Figure 5.1 illustrates the existing experimental setup to test the inertia driven CPA with the DH-CVT. The experimental setup mainly consist of the flywheel as an input inertial energy storage element, the continuous variable transmission to transmit the energy in a controlled way, the torque actuator that provides the actuation torque to achieve the desired load motion. It is controlled separately from the energy source and a disc shaped load at the output.

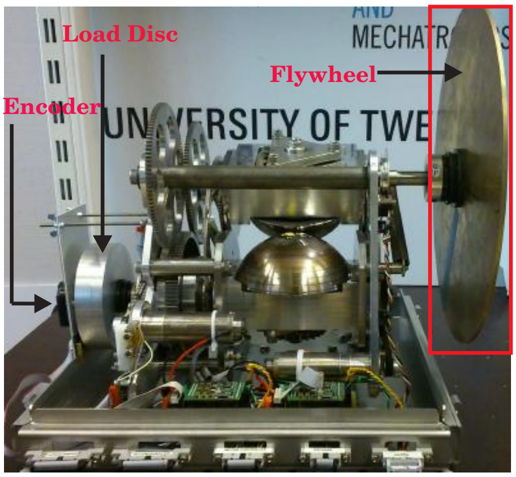

Figure 5.1: Experimental setup

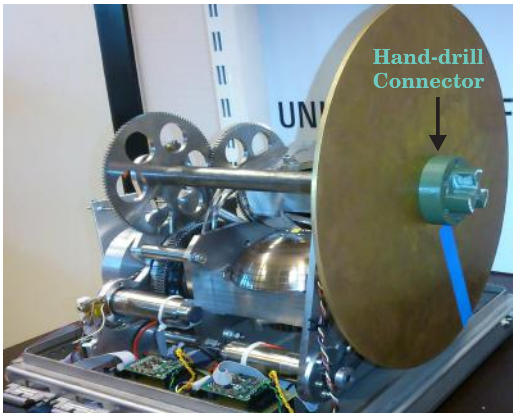

Figure 5.2: Hand drill connector

Additionally, an incremental encoder is placed at the output of the setup to measure the load position, see Figure 5.1. Details about the encoder are mentioned in Appendix B.1. Moreover, a connector composed of the light weight material 'ABS' is attached to the flywheel to connect the hand-drill externally scuh that the flywheel rotation would be possible in order to store energy, see Figure 5.2.

Figure 5.3 indicates the sensors placed on the actual experimental setup. Sensors placed at the input, output and reconfiguration motor measures the input position, output position and the reconfiguration mechanism position respectively. They provide the position feedback to the position (servo) and ratio controller. Similarly, the flywheel velocity feedback is provided to the torque control block by taking derivative of the flywheel position feedback obtained from the sensor placed at the input. The interfacing model developed in the 20-sim 4C allows to operate the controllers with the help of sensors.

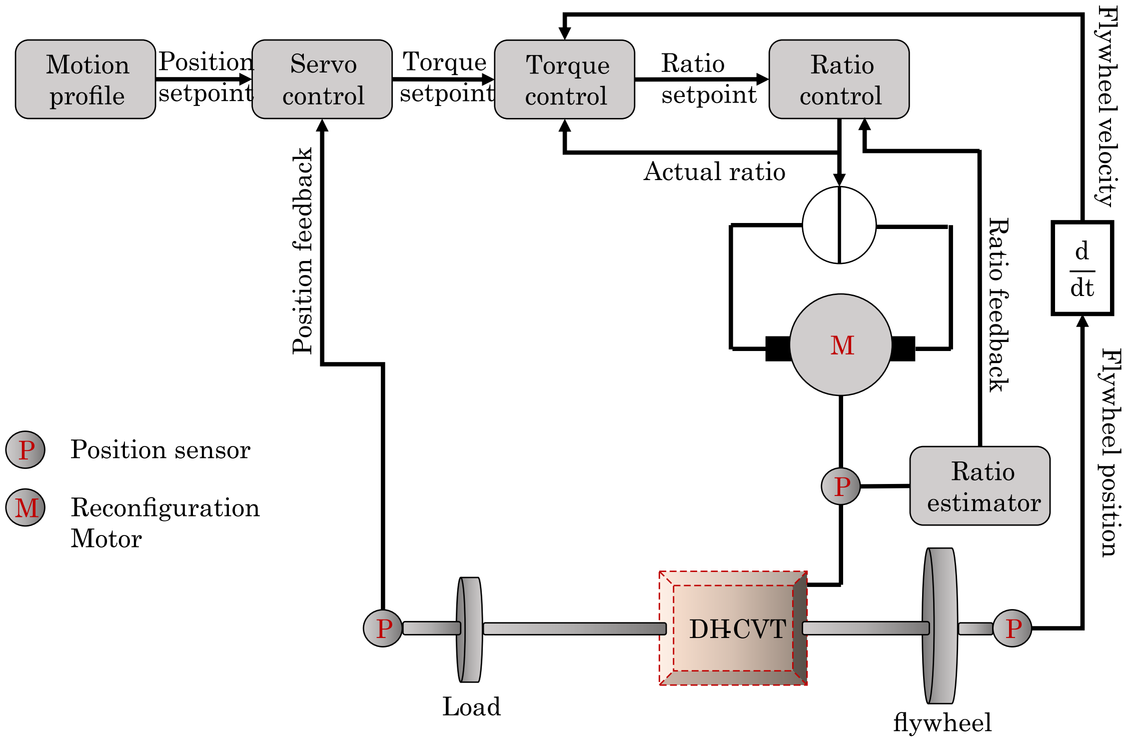

Figure 5.3: Schematic overview of the DH-CVT experimental setup with control layers

5.2 Experiment design: Inertia Driven CPA

The main purpose of this assignment is to demonstrate the inertia driven CPA with the DH-CVT. In this experiment, we apply a DH-CVT with an inertia (flywheel) as a torque actuator to change the state of the load as an alternative to an electric actuator to supply the required energy to the system.

Specifically, the aim of this experiment is to provide the controlled transmission of the stored energy in the flywheel to the load with the help of the DH-CVT to achieve the desired load motion.

The objectives to achieve in this experiment are to store the required energy in the flywheel and vary the CVT transmission ratio in order to control the energy flow in the system, such that obtention of the desired output behavior can be achieved.

5.2.1 Procedure:

From the simulation results obtained in Chapter 4, a step by step procedure given below is describing the specific order in which experiment needs to be followed.
1. Connect the hand-drill to rotate the flywheel to approximately 350 RPM speed to store the required energy keeping the transmission ratio zero, avoiding the energy transmission to the load. (Measure the flywheel speed and time required to rotate the flywheel approximately to 350 RPM speed).
2. Disconnect the hand-drill as soon as the flywheel rotates approximately to the required speed. The energy in the flywheel will dissipate over time, as shown in simulations, and we expect there will be enough energy for the operation to pursue for approximately 25 seconds.
3. Control the ratio of the CVT to control the energy flow and achieve desired motion of the

load.
4. Observe the load motion and transmission ratio variation.

5.2.2 Expected observations:

Simulation observations and results provided insight for the expected observations for the Inertia driven CPA experiment. The following points are important to observe during the experiment in order to reach its positive conclusion.
• The required energy is stored in the flywheel at the transmission ratio zero.
• The transmission ratio is non-zero when the energy content in the load is changing and returns to zero when the energy content in the load is constant.
• When the load position changes, the kinetic (co)energy from the flywheel is converted to the kinetic (co)energy in the load and does not vary the kinetic co(energy) when the load stops moving.
• Eventually, due to the internal friction in the system; the energy stored in the flywheel is dissipated completely to move the system. How long the flywheel energy provides the desired load motion? How much energy is dissipated in average?

5.3 Inertia Driven CPA experimental findings

The DH-CVT setup consists of the reconfiguration mechanism and the drive-train mechanism. The energy transmission is done through the drive-train mechanism. In order to ensure the controlled transmission of the energy in the system, the ratio controller is developed for the reconfiguration mechanism (see Section 2.2.4). Thus, at the beginning, it is important to test the performance of the ratio controller throughout the transmission ratio range that will be used in the inertia driven CPA experiment later. To test, the ratio controller, the transmission ratio is varied starting at zero and modifying the values to either side of the range (-3.5 or 3.5) using different speed rates in between the changes. The results of this experiment is shown in Figure 5.4.

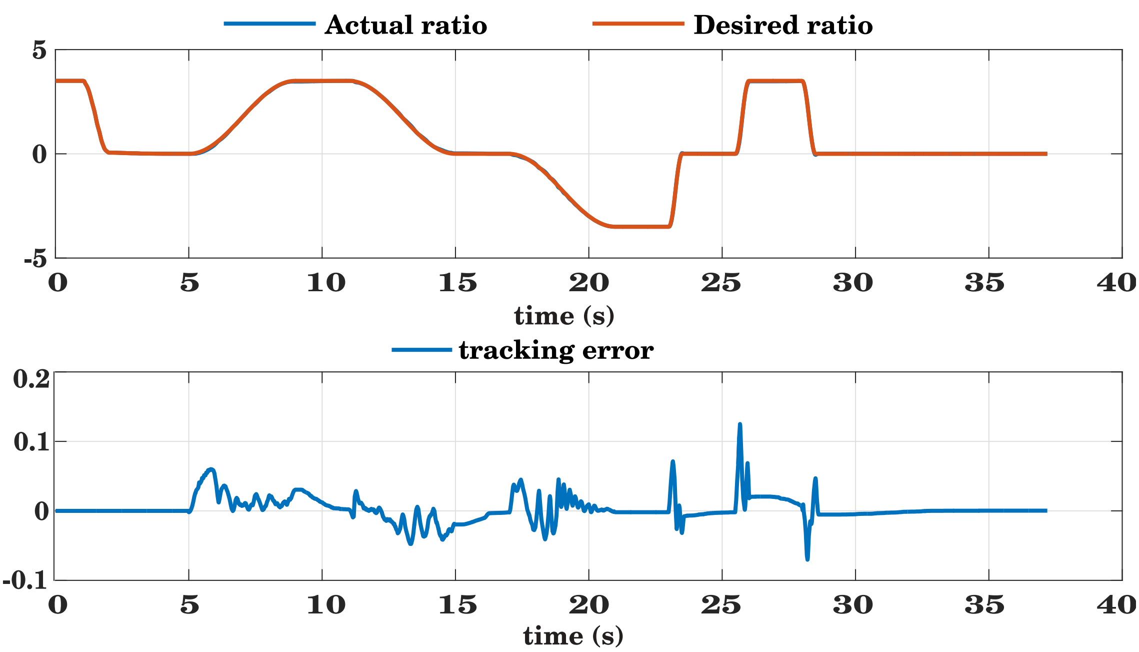

Figure 5.4: Ratio controller performance

The first two seconds in Figure 5.4 indicate the soft initialization procedure required to avoid the overshoot due to the abrupt change in the set-point at the beginning of the experiments in the DH-CVT. Figure 5.4 depicts the proper tracking performance of the ratio controller over the full range of the transmission ratio (Actual ratio and desired ratio signals are overlapping in the Figure 5.4 and tracking error is almost negligible). Hence it is possible to conclude that the performance of the ratio controller is as desired and useful in the Inertia driven CPA experiment.

Having done that, the experimental procedure described in Section 5.2 is followed. The inertia driven CPA experiment is executed in four phases in different time intervals, explained in Table 5.1.

Phase	Time (seconds)
Ratio initialization	0 - 2
Zero transmission ratio	2 - 10
Flywheel energy storage phase	4 - 10
DH-CVT system motion phase	from 10 onward

Table 5.1: Inertia driven CPA: experiment phases

During the first phase (ratio initialization) of two seconds, the ratio initialization procedure is done to avoid the abrupt overshoot preventing the mobile sphere from hitting the end top, this can be seen in Figures 5.4 or 5.6. Then, during the second phase (zero transmission ratio) of 2 to 10 seconds, the transmission ratio is kept zero to allow the energy storage in the flywheel by avoiding the energy transmission in the system before motion of the system. Next, the flywheel energy storage phase lasts between 4 to 10 seconds, in which the flywheel is rotated to store a sufficient amount of energy. After storing the energy in the flywheel, in the final phase, the system's motion starts at 10 seconds - using the energy from the flywheel. Next, the results obtained for the inertia driven CPA experiment are explained in detail.

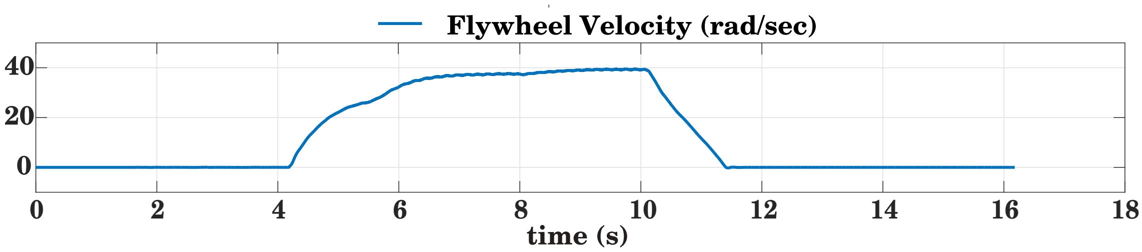

Figure 5.5: Inertia driven CPA experiment: Flywheel rotation

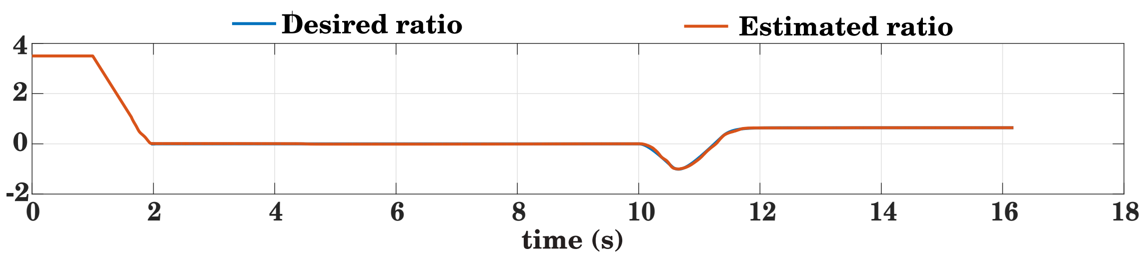

Figure 5.6: Inertia driven CPA experiment: Transmission ratio tracking

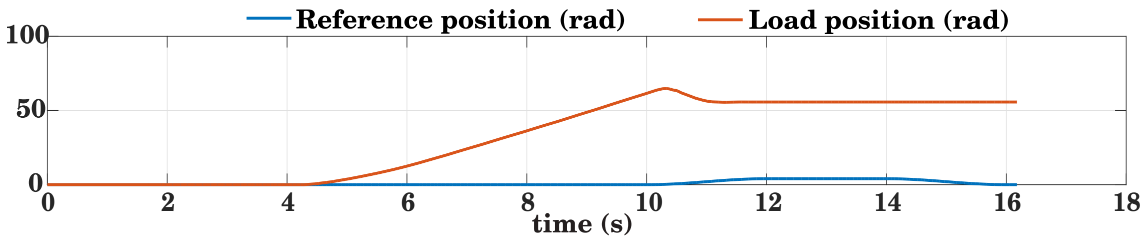

Figure 5.7: Inertia driven CPA experiment: Load position

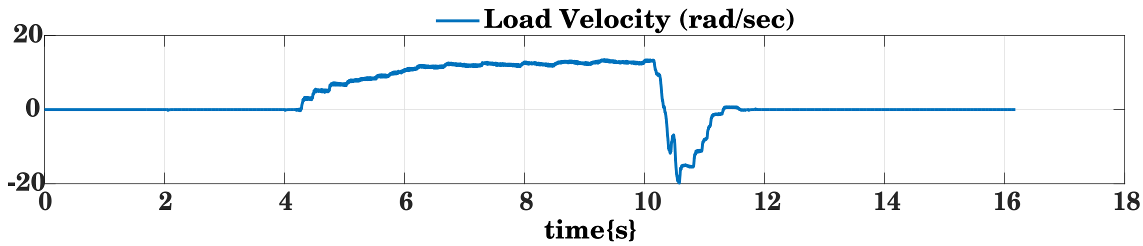

Figure 5.8: Inertia driven CPA experiment: Load velocity

Figure 5.5 shows that the flywheel is rotated with the help of a hand-drill up to 350 RPM (*visible as ≈ 36 rad /sec*)during flywheel energy storage phase, which is also a zero transmission ratio phase. Thus, the transmission ratio during this period is zero, see Figure 5.6. After 10 seconds, the hand-drill is removed so that the energy stored in the flywheel is transmitted to the system by controlling the transmission ratio to achieve the desired load motion. Unfortunately, energy stored in the flywheel lasts only for 1.5 seconds, not enough to observe the expected behavior of the load.

Figure 5.7 depicts the picture of the load motion during the energy storage phase (*4 to 10 seconds*) and DH-CVT system motion phase (*after 10 seconds*). It can be clearly seen that the load starts moving as soon as the flywheel starts rotating at 4 seconds (*see Figure 5.5*) which is undesired and unexpected. Besides, the transmission ratio is still zero which is desired and expected. That means the actual experimental ratio is contrasting to the estimated transmission ratio. The conflict between this expected and unexpected result arose the suspicion that there is an error in the system to achieve the transmission ratio. Figure 5.8 shows the load velocity behavior.

5.3.1 Detailed discussion and results

In the beginning, to get the enough time to store the required energy in the flywheel, the DH-CVT system motion time is set after 10 seconds. Thus, after the soft initialization of first two seconds, a signal is passed to the system to make the transmission ratio zero until 10 seconds with the help of the ratio controller (see Figure 5.6 - depicting the good ratio tracking performance of the ratio controller). This provides us a sufficient time (period of almost 8 seconds) to speed up the flywheel at transmission ratio zero to store the energy. In this period, the flywheel is rotated from 4th second to the 10th second to achieve the desired 350 RPM speed (≈ 36 rad /sec) with the help of a hand-drill(see Figure 5.5).

Before the system motion time, it is expected that the load remains still since it is not desired to have the energy transmission during flywheel energy storage. It is seen that the desired / actual transmission ratio obtained from the ratio controller is almost zero before the system motion time. The ratio controller controls and measures the desired reconfiguration motor angle and provides the desired ratio using that angle. The relation that calculates the desired ratio from the desired angle is given as (Dresscher et al., 2016):

$$r_{ps} = \frac{-r_{fr}^2(1+X) + X tan(\phi)}{r_{fr}^2} \tag{5.1}$$

Where, r_{ps} = estimated/desired ratio
r_{fr} = fixed gear ratio
X = planetary gear constant
ϕ = reconfiguration motor angle

Despite observing that the zero transmission ratio is achieved, which was desired, Figures 5.7 and 5.8 show the unexpected load motion before set system motion time ($10 seconds$) which suggested that the actual experimental ratio is different than the desired one. These figures illustrate that the load starts moving as soon as the flywheel start accelerating, meaning that the load cannot stay at still position during the flywheel's energy storage time. This is due to the fact that the actual experimental ratio is different from the desired ratio reading that is obtained from the ratio controller. It can be confirmed by calculating the actual experimental ratio, considering the ratio of the load velocity and flywheel velocity. The data-points are taken at the 9th second, and the experimental ratio is calculated below. This is an alternative analytical relation allowing to calculate the value of the transmission ratio.

$$\text{Measured ratio (Experimental ratio)} = \frac{\text{Load Velocity}}{\text{flywheel Velocity}} = 12/40 = 0.3 \tag{5.2}$$

The calculation above shows that the transmission ratio which was desired to be zero before starting the system motion is actually 0.3. Practically, the ratio obtained from the ratio controller (i.e. desired ratio calculated from Equation 5.1) and the experimental ratio (calculated from Equation 5.2) should be similar. This inspection suggests that there might be an issue in the mechanical system of the DH-CVT, making it difficult to achieve the desired transmission ratio and thus making it practically impossible to achieve the successful results for the inertia driven CPA experiment at the current stage. However, the reading was taken only for the one data-point and this is just an hypothesis. Hence, a detailed analysis is required to understand the problem. More experiments are conducted to investigate the cause of the error occurring in the desired and experimental transmission ratio, see Section 5.4.1 and 5.4.1.

An additional important factor encountered during the experiment is that the energy in the flywheel drained much faster than anticipated (within 1.5 seconds - see Figure 5.5). Hence, it is expected that the internal friction in the system is significantly higher than the considered friction during the simulation. Apart from the obvious friction during the system motion, the mechanical system of the DH-CVT also exhibits the friction during the energy storage phase. Friction during the energy storage phase is due the the fact that the flywheel rotates along with the other parts of the system such as planetary gear, fixed gears and the CVT hemispheres as well, since they are directly coupled to each other. Non-zero velocity of the other parts of the system during the flywheel energy storage phase increases the mechanical losses. It makes the energy storage inefficient. Unfortunately, the friction in the simulation in Section 4.7 is placed after the CVT transmission, and as a result, it accounts for the friction only when the system is in motion i.e. when energy is transmitted to the load and neglects the friction during the flywheel energy storage phase and at the transmission ratio zero. The solution could be to place the friction at the input, since it is fundamentally identified at the input of the system (Dresscher et al., 2016). Revised simulation results are already presented in Section 4.8 of Chapter 4.

Using the revised friction behavior in the system, it would be possible to design the required flywheel to provide sufficient energy to the DH-CVT system to drive the load. The solution could be to add a small motor at the input, which should compensate for the friction losses in the system. This should allow us to reduce the heavy and high speed flywheel model to a sensible model. Moreover, this should increase the working efficiency of the Inertia driven system. This nevertheless, is not in the scope of this assignment.

5.4 Further analysis and results

In this section, a detailed analysis is done to understand the cause from which the problem arose during the inertia driven CPA experiment. More experiments are conducted to learn about the exact cause of the unexpected behavior of the transmission ratio - explained in Section 5.4.1 and Section 5.4.1.

5.4.1 Experiment 2: To find the cause of error in the transmission ratio

This experiment was conducted in order to understand the cause of error which exists between the desired ratio and experimental (measured) ratio. In this experiment, the reconfiguration angle is varied over its full range and the correspondence between the desired ratio and experimental ratio are obtained. The plot of reconfiguration angle versus the desired ratio and the experimental ratio gives a better insight about the problem causing the deviation of the experimental ratio from the desired ratio, as shown in Figure 5.9.

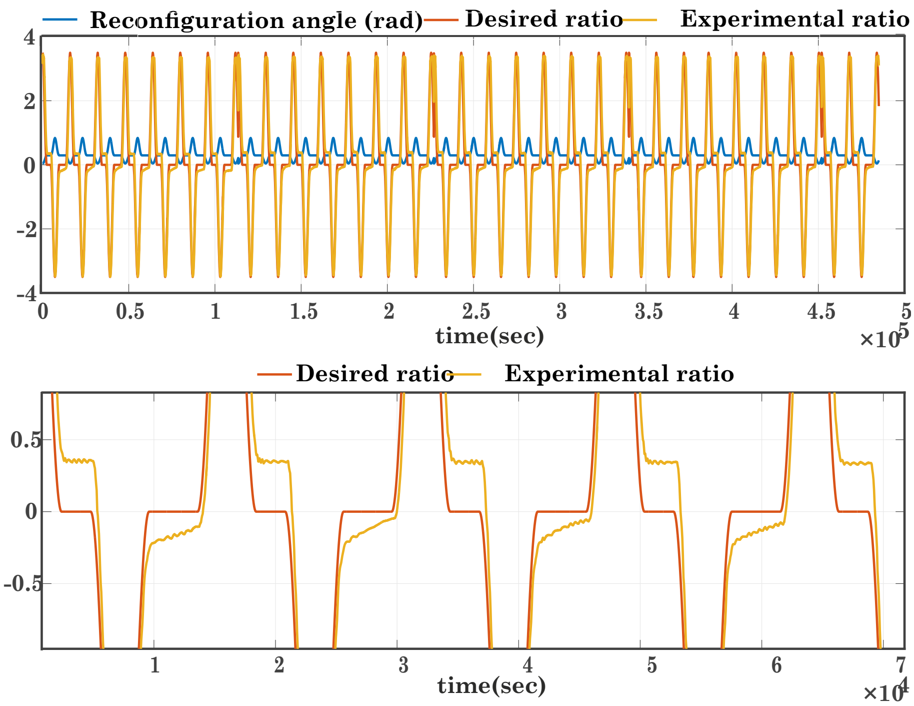

Figure 5.9: Hysteresis effect around transmission ratio zero

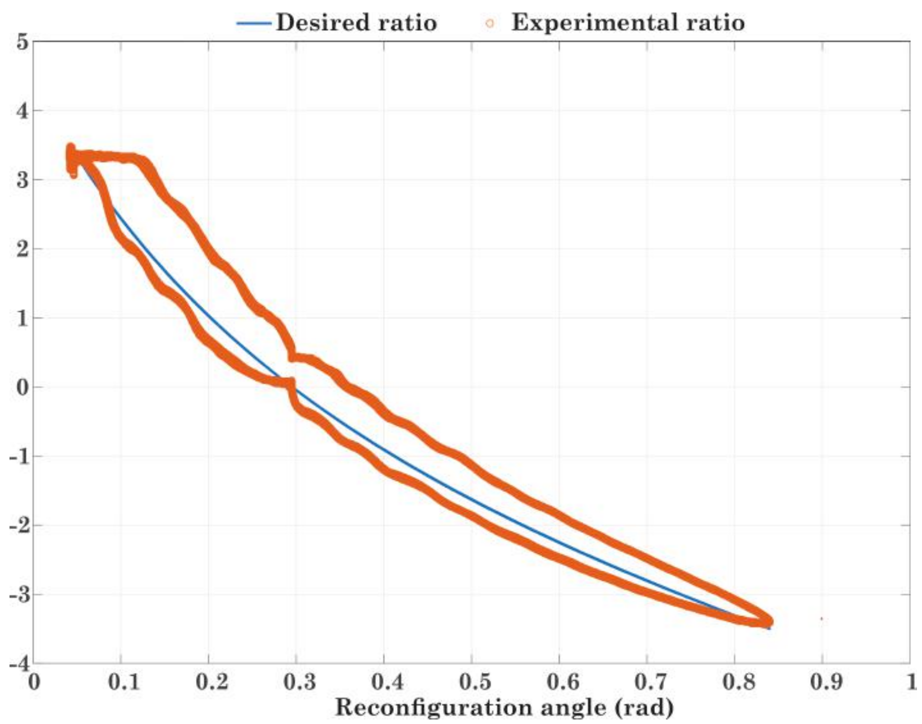

Figure 5.10: Full transmission range -3.5 to 3.5: Hysteresis shape

It can be clearly observed in Figure 5.9 that the experimental ratio follows the desired ratio with an insignificant phase delay for the full range of transmission ratio. The delay in the system might be due to the dynamics of the system. Most importantly, the plot shows that there is an hysteresis effect around the transmission ratio 0, restricting the system to achieve an exact zero transmission ratio which, in turn, affects the performance of the state of the system - Figure 5.7. This can be caused by backlash effect or elastic deformation, but is mainly due to high frictional effects in our highly non-linear system. These effects implies that the hysteresis is restricting the system to achieve the desired transmission ratio.

Now that we know the cause of the problem, our hypothesis is that at least part of the error shown in Figures 5.9 and 5.10 is caused by the hysteresis. In the next section, an experiment is discussed to test this.

Hypothesis: The static hysteresis is present at the sphere angle of the DH-CVT, causing the significant difference between the motor angle and the sphere angle and is hence restricting the system to achieve the desired transmission ratio.

Experiment 3: To validate the hypothesis that the static hysteresis is present between the reconfiguration sphere angle and the reconfiguration motor angle

This experiment is conducted to justify the hypothesis mentioned in the previous section. The presence of static hysteresis between the reconfiguration sphere angle and the reconfiguration motor angle would mean that the exact location of the hysteresis is located at the output i.e. at the sphere angle, otherwise it would mean that more research is needed to detect the hysteresis in other parts of the system.

Figure 5.11 is the composite representation of the static hysteresis. It indicates that the hysteresis at the sphere angle causes the difference between the CVT desired ratio and the experimental ratio. If the static hysteresis is not modeled and compensated, the hysteresis loop contributes an input uncertainty to the CVT, which was encountered during the inertia driven CPA experiment.

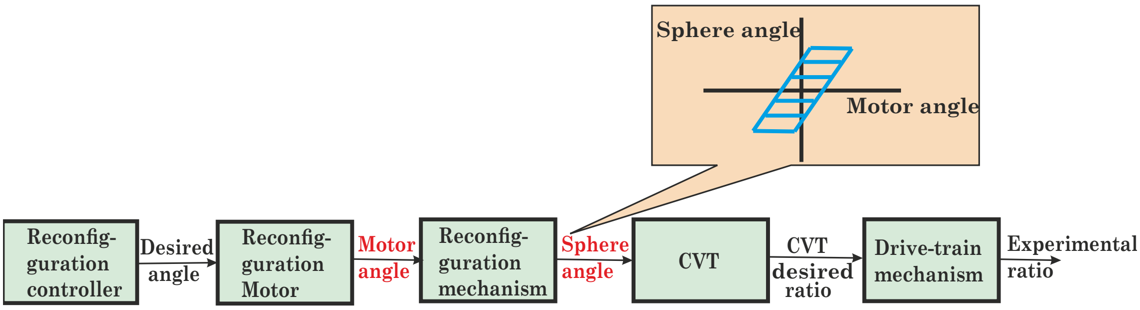

Figure 5.11: Composite representation of the static hysteresis

In this experiment, the reference to the motor angle, which is input to the reconfiguration system, is varied and the flywheel is accelerated to provide the energy using the given transmission ratio (desired ratio) such that the load motion can be observed. The experimental ratio is recorded for the desired ratio (input). The experimental ratio is calculated by taking the ratio between the load velocity and the flywheel velocity. Finally, the corresponding sphere angle (output) is calculated using Equation 5.1.

Steady state is considered for each ratio, at the interval of 0.5, for the full range of transmission ratio (-3.5 to 3.5). This would provide the static hysteresis present at the output (i.e sphere angle) for the full range.

Figure 5.12 depicts the difference identified between the desired ratio and the experimental ratio. i.e. It actually shows that the system is restricted to achieve the desired transmission ratio. It motivates that the static hysteresis is indeed present between the motor angle and sphere angle, and that a direct relationship between them is not of easy task.

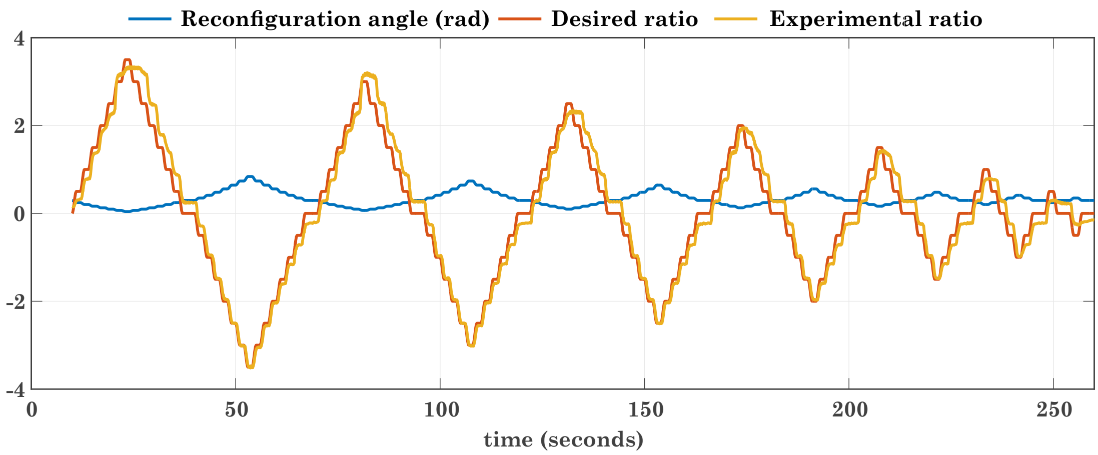

Figure 5.12: Static hysteresis over the full transmission ratio range

Figure 5.13 clearly shows the static hysteresis behavior between motor angle and sphere angle over the full range of the transmission ratio.

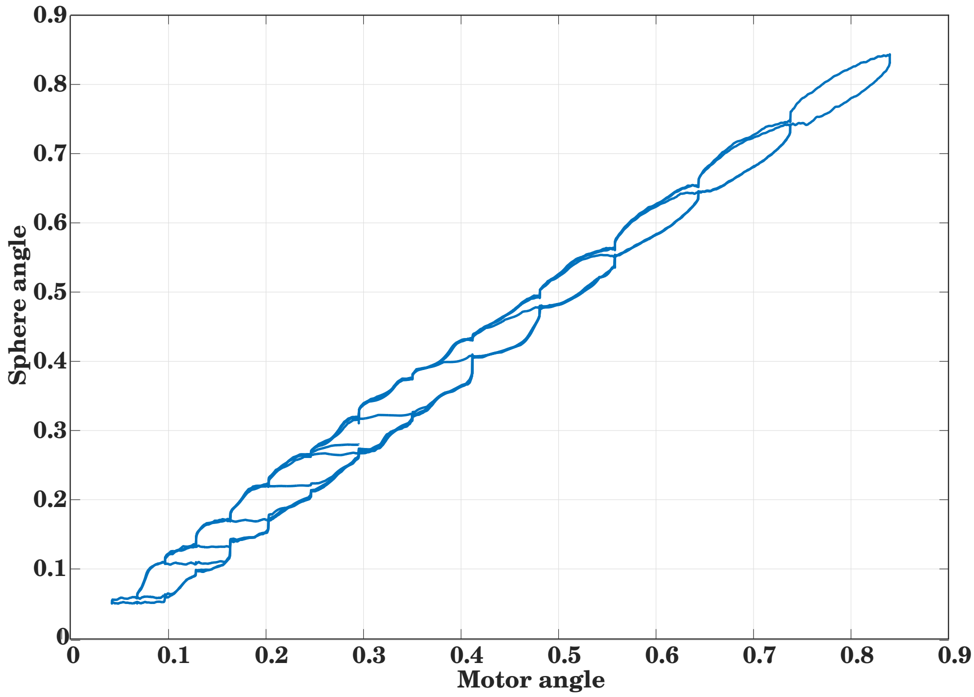

Figure 5.13: Static hysteresis between motor angle and sphere angle

Above mentioned plots justify the hypothesis made at the end of Section 5.4.1. The unexpected significant difference between the desired and experimental ratio show significant effect on the performance of the load for the inertia driven CPA experiment - Figures 5.7 and 5.6. Thus, the hysteresis is quite significant. Ultimately, the identified hysteresis phenomena in the DH-CVT mechanical setup concluded that it is not possible to achieve the desired transmission ratio with sufficient accuracy, required to successfully demonstrate the Inertia driven CPA experiment, the main aim of this research. Hence, more research is required prior to the inertia driven CPA experimental demonstration.

6 Conclusions and Recommendations

6.1 Final discussion and conclusion

Significant energy loss occurs by using electrical actuators in legged locomotion of walking robots. In order to develop energy efficient walking robots by providing an efficient actuation method as an alternative to electrical actuators, this research focused on the development of Inertia driven controlled passive actuation with the DH-CVT.

To accomplish the goal of this research, first, a comprehensive IPM was created for the already existing overall DH-CVT system that demonstrated the key functionality of the system. Henceforward, the flywheel inertia and velocity parameters were roughly estimated using the repeated simulation of the IPM. Simultaneously, the geometrically feasible flywheel was designed accordingly.

Next, the designed modified PD controller (servo controller) provided the stable performance illustrating acceptable path tracking and better noise rejection in the simulations. Consequently, we have shown that we can separate the energy source mechanism from the servoing mechanism. Not to mention, the gradual dissipation of energy due to the friction in the system also exhibited that the flywheel provided sufficient amount of energy to drive the load. It proved that the flywheel design is acceptable, feasible and ready to manufacture. Finally, the experimental setup is prepared by incorporating the manufactured flywheel (input) and disc shaped load (output) in the existing DH-CVT system.

Most importantly, the simulation results concluded that the load can be actuated by the energy stored in the Inertia (flywheel) and the controlled energy transfer is achieved with the help of the DH-CVT. Naturally, it implied that the Inertia driven controlled passive actuation with the DH-CVT can be demonstrated in practice. The inertia driven CPA experiment is then designed accordingly.

Moving forward towards our research goal, The inertia driven CPA experiment was demonstrated and the findings showed that:
1. The fast drained flywheel energy during the DH-CVT system motion phase and acceleration of the flywheel with other parts of the system during the energy storage phase suggested that the friction in the system is significantly higher than the friction that was considered in the simulations. It implied that storing the non-zero amount of energy requires a non zero velocity. We know that the mechanical losses only occur at a non zero velocity. Therefore, it is concluded that storing the energy is inherently associated with the mechanical losses and hence a less efficient process, initially expected to be more efficient. It is also implied that the friction location in the system provides inadequate insight of the overall friction in the system and hence has to be remodeled and replaced at the correct place.
2. The unexpected behavior of the load and significant difference between the desired ratio and the experimental ratio (measured ratio) lead us to conclude and hypothesize that there is an issue in the mechanical system which has restrained the system to achieve the desired ratio and thereby achieve the desired load motion. Ultimately, applying the the inertia driven CPA, achieving the good performance with high efficiency has proven to be difficult at the current stage of this research. Substantially, further research was needed to find the cause of the error in the system. Here, the hypothesis replaced the aim of this research.

Further research gave us new insight that the significant static hysteresis loop is present between the reconfiguration sphere angle and the reconfiguration motor angle. It has restricted the system from achieving the desired transmission ratio. This justified the previous hypothesis. The hysteresis possibly have occurred due to elastic deformation, backlash and high friction phenomena in the existing DH-CVT system. Therefore, newly encountered hysteresis phenomena implicated that the issue is in the mechanical design of the DH-CVT.

Ultimately, having the aim of developing efficient way of actuation, i.e the inertia driven controlled passive actuation with the DH-CVT, resulted in finding out new insight that was unknown to us before, i.e static hysteresis is present in the DH-CVT system and it is necessary to be counteracted in order to achieve the successful demonstration of the inertia driven CPA.

6.2 Recommendations for future work

Based on this thesis, we have some recommendations for future work:

1.Before demonstrating the inertia driven CPA experiment again, it is recommended to counteract the hysteresis phenomenon present between the sphere angle and motor angle of the reconfiguration mechanism.

Possible solutions:
A. The mechanical system can be redesigned. However, it is a complex, time consuming and costly option.
B. Applying a control action. Since the static hysteresis is present at the sphere angle (at output) of the reconfiguration mechanism, it should be possible to achieve the solution by inverting the hysteresis model at the motor angle (at input) of the reconfiguration mechanism. This could compensate the hysteresis effect allowing the system to achieve the desired transmission ratio (see fig. 6.1).

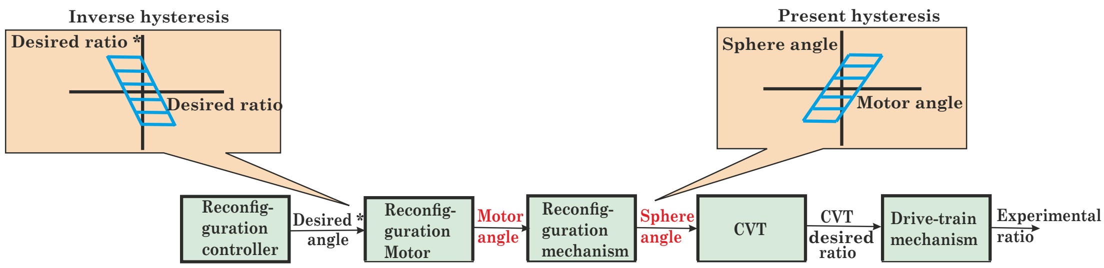

Figure 6.1: Composite representation of the static hysteresis solution

An inverse feed-forward controller could be developed to provide the solution. The following research papers suggest developing the solution by applying a feed-forward controller:

Reference: (Qingsong Xu and Yangmin Li, 2011)

Extensive research has been carried out for the modeling and control of hysteretic non-linearity in the past two decades. Both feed-forward control and feedback control approaches have been investigated. Since feed-forward control does not affect the stability of the system, it is employed widely. Feed-forward compensation can be implemented by solving an inverse function based on an hysteresis model ((Qingsong Xu and Yangmin Li, 2011)).

Reference: (Hassan Sayyaadi, 2012)

Literature review of the research conducted in this area shows that using the inverse of the phenomenological hysteresis models can compensate the hysteresis effectively. The generalized Prandtl-Ishlinskii model is analytically invertible, and therefore can be implemented conveniently as a feed-forward controller for compensating hysteresis non-linearities effects. The feed-forward part of the control system can be developed using the generalized Prandtl-Ishlinskii inverse model while, a conventional proportional integral feedback controller can be added to the feed-forward controller to increase the accuracy together with eliminating the steady state error in position control process. 6.1)

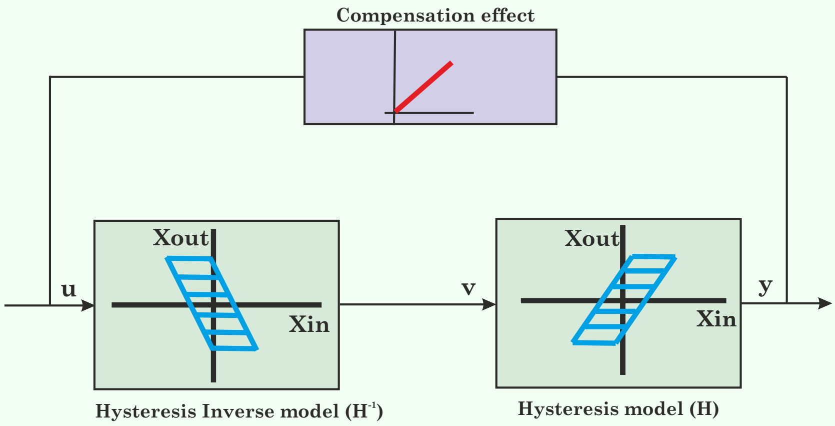

Figure 6.2: Solution: Compensation of actuator hysteresis by exact inverse model

Compensation effect by inverse hysteresis model is shown in figure 6.2. Generally, as shown in Fig. **??**, for the hysteresis model H and hysteresis inverse model H^{-1}, the following equation can be obtained if the exact inverse compensated H^{-1} exists.

$$\{y = H(v) = HH^{-1}(u) \longrightarrow HH^{-1}(\cdot) = I\} \Longrightarrow y = u \tag{6.1}$$

where y is the output of the generalized Prandtl Ishlinskii model, u and v, are respectively the input and output of the generalized Prandtl Ishlinskii inverse model.
For detailed study of inverse feed-forward controller, (Guo-Ying Gu, 2012) could also be useful.

2. It would be more beneficial if the decoupled friction models are developed for input and output separately.

3. A small motor can be integrated in the system to compensate only for the friction energy losses. Consequently it should allow to obtain a reliable flywheel model for the existing DH-CVT system .

4. Since, the simulation results provided the acceptable insight for the expected key behavior of the actual physical system, it is recommended to use the same approach for developing the flywheel model by incorporating the decoupled input and output friction models in the simulation and then demonstrate the inertia driven CPA experiment again.

A Appendix 1

A.1 Dual-Hemi CVT Drive-train mechanism elements in detail

Element	Value
Hand-drill (as source of Torque) T	-
Flywheel inertia I_f	0.0155 kgm^2/rad
Flywheel mass m_f	1.55 kg
Inertia of secondary gear I_{scg}	5.226×10^{-6} kgm^2/rad
Inertia of safety clutch + shaft + sun gear I_{sng}	1.8823×10^{-5} kgm^2/rad
i_3	7.925 mm
Stiffness between teeth of sun and planet gears	∞
i_4	1/10 $1/mm$
Inertia of planet gears I_{ptg}	3.693×10^{-6} kgm^2/rad
i_5	10 mm
Stiffness between teeth of ring and planet gears	∞
i_6	1/28.15 $1/mm$
Inertia of the carrier (cage) I_{cage}	2.7255×10^{-5} kgm^2/rad
Inertia of the ring gear I_{rgg}	1.1663×10^{-4} kgm^2/rad
Stiffness of shaft from ring gear to crown gear$_1$	17766.638 Nm/rad
Inertia of crown gear$_1$ I_{cng1}	1.2021×10^{-4} kgm^2/rad
i_7	30.25 mm
Stiffness between teeth of gears	∞
i_8	1/31.413 $1/mm$
Inertia of spur gear$_1$ + sphere$_1$ + its shaft I_{sp1}	1.5841×10^{-3} kgm^2/rad
CVT with unknown stifness and variable transmission ratio	-
Inertia of spur gear$_2$ + sphere$_2$ + its shaft I_{sp2}	1.5745×10^{-3} kgm^2/rad
i_9	31.413 mm
Stiffness between teeth of gears	∞
i_{10}	30.25 $1/mm$
Inertia of crown gear$_2$ I_{cng2}	1.2778×10^{-4} kgm^2/rad
Stiffness of shaft from crown gear$_2$ to spur gear$_3$	362.368 Nm/rad
Inertia spur gear$_3$ I_{spg3}	4.891×10^{-4} kgm^2/rad
i_{11}	60.5 mm
Stiffness between teeth of gears	∞
i_{12}	1/60.5 $1/mm$
Inertia of spur gear that connects to cage I_{gcg}	1.1685×10^{-3} kgm^2/rad
i_{13}	60.5 mm
Stiffness between teeth of gears	∞
i_{14}	1/60.5 $1/mm$
Inertia of spur gear output + output shaft I_{gout}	5.2974×10^{-4} kgm^2/rad
Stiffness of output shaft	47909.287 Nm/rad
Load inertia I_{load}	6.3 $\times10^(-4)$ kgm^2/rad
Load mass m_l	0.5 kg

Table A.1: Elements in the DH-CVT drive-train mechanism & their values

A.2 Dual Hemi CVT reconfiguration mechanism elements

Element	**Value**
Motor (as source of Torque) T	-
Motor inertia I_m	$2.12\times10^{-6}\ kgm^2/rad$
Gearbox ratio	1:35
Gearbox Inertia I_{gb}	$1.7692\times10^{-7}\ kgm^2/rad$
Belt drive input ratio	4.9 mm
Timing belt stiffness C_{tb}	7500000 N/m
Belt drive input ratio	1/28.22 $1/mm$
Inertia of secondary gear of belt drive	$3.45035\times10^{-6}\ kgm^2/rad$
Length of lever	120 mm
Mass of mobile sphere module M_{sph}	4.5 kg
Stiffness of gravity compensator spring C_{gc}	1800 N/m
Rolling friction between spheres R_s.	3.2

Table A.2: Elements Reconfiguration mechanism elements and their values

B Appendix 2

B.1 SOLIDWORKS 2D drawings

In this section, SOLIDWORKS 2D drawings that are made for manufacturing the flywheel (input) and disc shaped load (output). These parts are used in the inertia driven CPA experiment.

Flywheel 2D drawing

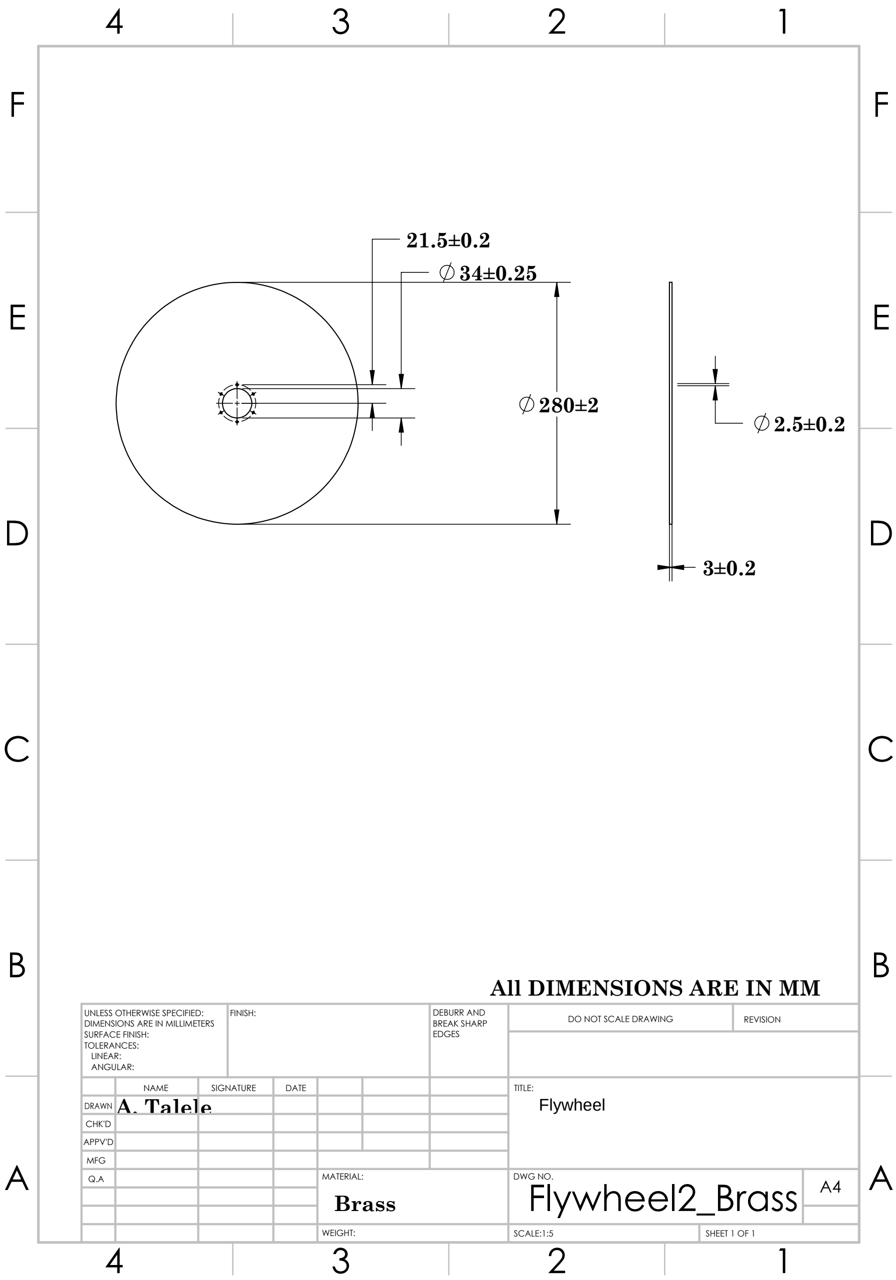

Figure B.1: Flywheel model for Inertia Driven CPA experiment

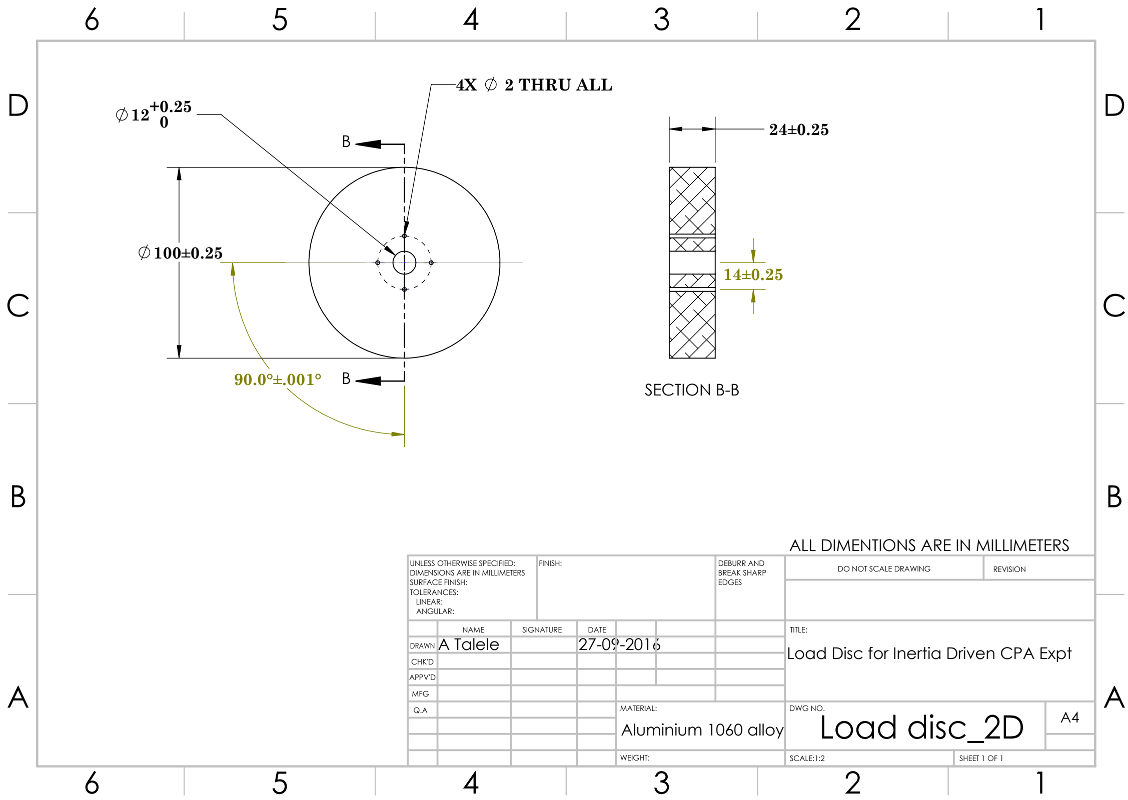

Figure B.2: Disc shaped load model for Inertia Driven CPA experiment

B.2 Output encoder placement

HEDL-5540#A13 ENCODER, ROTARY, 500PPR, 3CH

It is also important to ensure the newly placed encoder performance and to measure the number of counts in order to calculate the load position in radians. To measure number of counts per revolution, the load disc is rotated for one revolution manually and load disc encoder reading is recorded. The figure B.3 shows the number of counts per revolutions. 1 revolution = 2000 counts

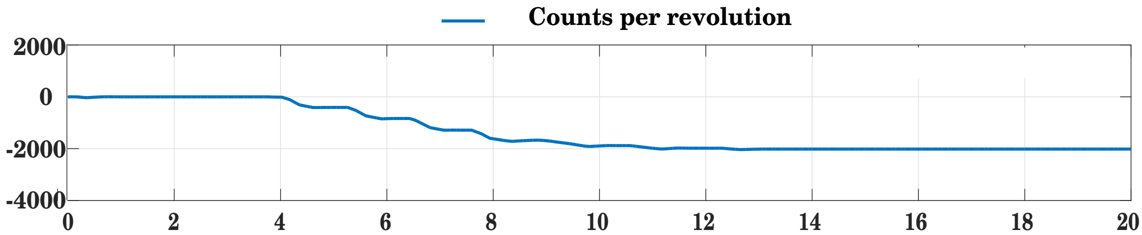

Figure B.3: Output encoder check and number of counts per revolution

Relation used:

$$\text{Load position (in radians)} = \frac{\text{Load position (in counts)}}{\frac{\text{counts per revolution}}{2\pi}} \tag{B.1}$$

Bibliography

Astrom, K. J. (2002), *Control System Design, Chapter 5 feedback fundamentals*, Department of Mechanical and Environmental Engineering University of California Santa Barbara.

Bonilla, A. (2016), Controller design for Dual-Hemi CVT, Technical report, University of Twente, The Netherlands.

Coelingh, H. J. (2000), Design support for the motion systems, A mechatronic approach, Technical report, Universiteit Twente, Netherlands.

Collins, S. H., M. Wisse and A. Ruina (2001), A Three-Dimensional Passive-Dynamic Walking Robot with Two Legs and Knees, Cornell University, USA, Delft University, Netherlands.

Dresscher, D., M. Naves, T. J. de Vries, M. Buijze and S. Stramigioli (2016), Power split based dual hemispherical continuously variable transmission, University of Twente.

Dresscher, D. and S. Stramigioli (2013), Towards Controlled passive actuation, University of Twente.

Dresscher, D., T. J. de Vries and S. Stramigioli (2014), On energy losses in legged locomotion, University of Twente.

Dresscher, D., T. J. de Vries and S. Stramigioli (2015), Inertia-Driven Controlled Passive Actuation, in *ASME 2015 Dynamic systems and Control conference*, American Society of Mechanical Engineers.

Guo-Ying Gu, M. Y. (2012), Real-time inverse hysteresis compensation of piezoelectric actuators with a modified Prandtl- Ishlinskii model, State Key Laboratory of Mechanical System and Vibration, School of Mechanical Engineering, Shanghai Jiao Tong University, Shanghai 200240, China.

Hassan Sayyaadi, M. Z. (2012), Position control of shape memory alloyactuator based on the generalized Prandtl Ishlinskii inverse model, School of Mechanical Engineering, Sharif University of Technology, Tehran 11155-9567, Iran.

Jack A Collins, Henry Busby, G. S. (2010), *Mechanical Design of Machine Elements and Machines: A Failure Prevention Perspective, 2nd Edition*, https://books.google.nl/books?id=909-5C4eyUkC&pg=PA799&lpg=PA799&dq=flywheel+inertia+fits+the+feasible+mass&source=bl&ots=6SJC6iHDiU&sig=gXg_cB7KdacSEmxD9C56wyXuUxo&hl=nl&sa=X&ved=0ahUKEwi4q_CY1vHQAhWoIsAKHa6kAS0Q6AEIMTAB#v=onepage&q=flywheel%20inertia%20fits%20the%20feasible%20mass&f=false.

Kamf, T. (2012), High speed flywheel design, Technical report, Uppsala Universitet, Sweden.

Mcgreer, T. (1990), Passive dynamic walking, Simon Frazer University, Canada.

mitcalc (2016), Mechanical, Industrial and Technical Calculations, Springs calculation, 2016. [Online]., http://www.mitcalc.com/doc/springs/help/en/springs.htm.

Naves, M. (2014), Design of a continuously variable transmission for efficiently actuating walking robotic sensors, University of Twente.

Qingsong Xu, M. I. and S. m. I. Yangmin Li (2011), Modeling and Control of Rate-Dependent Hysteresis for a Piezo-Driven Micropositioning Stage.

Ragavan, A. J. (2012), STATISTICAL MODELING OF THE MECHANICAL BEHAVIOR OF SPRING, MASS AND DAMPER ASSEMBLY USING SAS, University of Nevada, USA.

de Vries, T. (2014), *Mechatronic Design of Motion Systems*, Robotics and Mechatronics, Utwente.